JOURNAL OF GEOPHYSICAL RESEARCH, VOL. 112, C11003, doi:10.1029/2006JC003819, 2007

A new approach to estimation of global air-sea gas transfer velocity fields using dual-frequency altimeter backscatter

Nelson M. Frew,[1] David M. Glover,[1] Erik J. Bock,[2,3] and Scott J. McCue[1]

Received 13 July 2006; revised 28 February 2007; accepted 2 June 2007; published 3 November 2007.

[1] A new approach to estimating air-sea gas transfer velocities based on normalized backscatter from the dual-frequency TOPEX and Jason-1 altimeters is described. The differential scattering of Ku-band (13.6 GHz) and C-band (5.3 GHz) microwave pulses is used to isolate the contribution of small-scale waves to mean square slope and gas transfer. Mean square slope is derived for the nominal wave number range 40–100 rad m^{-1} by differencing mean square slope estimates computed from the normalized backscatter in each band, using a simple geometric optics model. Model parameters for calculating the differenced mean square slope over this wave number range are optimized using in situ optical slope measurements. An empirical relation between gas transfer velocity and mean square slope, also based on field measurements, is then used to derive gas transfer velocities. Initial results demonstrate that the calculated transfer velocities exhibit magnitudes and a dynamic range which are generally consistent with existing field measurements. The new algorithm is used to construct monthly global maps of gas transfer velocity and to illustrate seasonal transfer velocity variations over a 1-year period. The measurement precision estimated from $>10^6$ duplicate observations of the sea surface by TOPEX and Jason-1 altimeters orbiting in tandem is better than 10%. The estimated overall uncertainty of the method is ±30%. The long-term global, area-weighted, Schmidt number corrected, mean gas transfer velocity is 13.7 ± 4.1 cm h^{-1}. The new approach, based on surface roughness, represents a potential alternative to commonly used parameterizations based on wind speed.

Citation: Frew, N. M., D. M. Glover, E. J. Bock, and S. J. McCue (2007), A new approach to estimation of global air-sea gas transfer velocity fields using dual-frequency altimeter backscatter, *J. Geophys. Res.*, *112*, C11003, doi:10.1029/2006JC003819.

1. Introduction

[2] The partitioning of biologically and climatically important gases between the surface ocean and the atmosphere is controlled by the complex interaction of multiple processes, principally biological production and consumption within the water column, solubility and diffusivity changes driven by temperature and salinity variations, vertical advection, and direct and bubble-mediated gas transfer across the air-sea interface. The relative importance of these processes varies both spatially and temporally. A quantitative treatment of air-sea gas fluxes is hampered by our current limited understanding of relationships between physical forcing and gas transfer rates. The combining of observed oceanic pCO_2 distributions [*Takahashi et al.*, 2002] and gas transfer velocity fields predicted by various parameterizations based on wind speed [*Liss and Merlivat*, 1986; *Wanninkhof*, 1992; *Wanninkhof and McGillis*, 1999; *Nightingale et al.*, 2000a, 2000b] leads to widely varying estimates of zonal and global net carbon fluxes [*Etcheto and Merlivat*, 1988; *Boutin and Etcheto*, 1995; *Boutin et al.*, 2002; *Wanninkhof et al.*, 2002]. Uncertainty in the gas transfer velocity parameterization is large (on the order of ±50%) and the choice of the gas exchange parameterization is now a significant term in the total error budgets of global carbon cycle models [*Takahashi et al.*, 2002; *Olsen et al.*, 2005].

[3] There are currently several approaches to the use of remote sensing observations to estimate gas transfer velocity, k, ranging from empirical parameterizations with wind or white cap coverage [*Boutin et al.*, 2002; *Erikson*, 1993; *Asher et al.*, 1998], to more physically based models that incorporate known transfer processes [*Soloviev and Schlüssel*, 1994; 2002; *Fairall et al.*, 2000]. The conventional approach is based on scatterometer or altimeter estimates of wind speed at 10 meter height, U_{10}, which is used with empirical gas transfer velocity-wind speed relationships to infer transfer velocity [e.g., *Boutin and Etcheto*, 1995; *Boutin et al.*, 1999, 2002]. These relationships [e.g., *Liss and Merlivat*, 1986; *Wanninkhof*, 1992; *Tans et al.*, 1990; *Wanninkhof and McGillis*, 1999; *Nightingale et al.*, 2000a, 2000b; *McGillis et al.*, 2001a, 2001b] were established primarily by relating field (lake and ocean) measurements of transfer velocity to anemometer winds observed from ships, buoys, and towers, adjusted to a 10 m height assuming a neutrally

[1] Woods Hole Oceanographic Institution, Woods Hole, Massachusetts, USA.
[2] Interdisciplinary Center for Scientific Computing, University of Heidelberg, Heidelberg, Germany.
[3] Deceased 25 June 2001.

0148-0227/07/2006JC003819$09.00

stable atmospheric boundary layer. Clearly, the generation of surface waves and subsurface turbulence by wind is the major process driving gas transfer [*Jähne et al.*, 1987; *Jähne and Haußecker*, 1998]. However, k does not depend simply on wind speed or wind stress [*Jähne et al.*, 1979, 1987; *Frew et al.*, 1995; *Frew*, 1997; *Hara et al.*, 1995; *Bock et al.*, 1999; *Wanninkhof and McGillis*, 1999; *Nightingale et al.*, 2000a]. Turbulence-enhanced gas transfer is influenced by many different factors, including the wind stress and its history, fetch-dependent wave age [*Wanninkhof*, 1992], wave-wave and wave-current interactions [*Coantic*, 1986; *Jähne et al.*, 1987; *Back and McCready*, 1988], atmospheric boundary layer stability [*Erikson*, 1993] and surface films [*Frew et al.*, 1990, 1995; *Bock et al.*, 1995; *Frew*, 1997; *Frew and Nelson*, 1999]. As a result, transfer velocity-wind speed parameterizations remain poorly constrained by field data, despite continuing field campaigns to study the air-sea exchange process.

[4] An alternative approach based on parameterization of the transfer velocity using altimeter-derived mean square surface slope, $\langle s^2 \rangle$, as a measure of sea surface roughness due to small-scale waves [*Frew et al.*, 1997; *Glover et al.*, 2002] is described herein. This approach attempts to relate transfer velocity more directly to wave-related processes of surface turbulence generation and surface renewal. Mean square slope is hypothesized to link gas transfer with key underlying processes including microscale breaking and wind stress-induced turbulence. As discussed below, the mean square surface slope for waves in the gravity-capillary wave number range appears to be a robust predictor of gas transfer velocity. An algorithm that utilizes normalized radar backscatter from the nadir-looking TOPEX and Jason-1 altimeters to estimate mean square wave slope has been developed. The mean square slope is scaled to gas transfer velocity using a relation between gas transfer velocity and mean square slope derived from field measurements of gas fluxes and small-scale wave slope spectra. The model function can be plotted against U_{10} as an index of convenience. It approximates currently used U_{10}-k relationships but differs in several important features and exhibits the expected scatter associated with variations in sea state. Using this empirical algorithm, monthly global estimates of k have been produced from the TOPEX and Jason-1 data streams.

[5] Derivations of operational global gas transfer velocity data products from scatterometry and from altimetry have several relative advantages and limitations. Scatterometers provide better spatial and temporal coverage than altimeters. The QuikSCAT SeaWinds scatterometer, for example, provides ~90% global coverage daily at 25 km resolution, whereas the TOPEX and Jason-1 altimeters are limited to narrow swath exact repeat ground tracks with 315 km spacing at the equator and ~10-day repeat coverage. Ground truth calibration of scatterometer wind speeds for use with k-U_{10} relationships is well established, while ground truth mean square slope measurements needed for validation of the altimetry-based estimates of k are sparse and difficult to make. On the other hand, ambiguity in the choice of k-U_{10} relation leads to widely varying flux estimates using scatterometer winds, whereas the dependence of transfer velocity on wave slope may be more robust than on wind speed. The TOPEX and Jason-1 altimeters provide a very long, stable record of radar backscatter cross section, from which mean square slope can be derived using a relatively simple scattering model. We describe this latter approach with the expectation that a mean square slope algorithm can be successfully extended to scatterometers observations as has been demonstrated by *Glover et al.* [2003, 2004].

2. Small-Scale Waves and Gas Exchange

[6] Recent field and laboratory studies have improved our understanding of the key role of small-scale waves in enhancing gas exchange. *Jähne et al.* [1984] first demonstrated the strong correlation between the gas transfer velocity for sparingly soluble gases and mean square surface slope and later hypothesized that energy put into the wavefield by the wind is transferred to near-surface turbulence enhancing gas transfer [*Jähne et al.*, 1987]. Subsequent work, discussed by *Frew et al.* [2004] has reinforced this hypothesis and demonstrated that k covaries strongly with the mean square slope of short wind waves. In situ air-sea interaction studies [*Bock et al.*, 1995; *Frew et al.*, 2004] have demonstrated the influence of sea surface films on both small-scale waves and near-surface turbulence. Surface films damp waves in the gravity-capillary and capillary range [*Bock and Mann*, 1989] and surfactant-induced reductions in wave spectral intensity in this wavelength range have been correlated with significant reductions in near-surface turbulence and gas transfer velocity [*Frew*, 1997; *Frew et al.*, 2004]. There have now been several mechanistic studies that have clearly demonstrated enhanced gas exchange due to breaking of small-scale waves without air entrainment, a process referred to as ''microscale wave breaking' or simply ''microbreaking' by *Banner and Phillips* [1974]. *Csanady* [1990] theorizes that the enhancement is due to turbulent surface renewal in the wakes of microbreaking waves and should be proportional to the fractional surface area of induced surface divergence. Regions of surface renewal due to microscale breaking of short wind waves (0.1–0.5 m) have been identified in IR imagery of laboratory wind waves by *Jessup et al.* [1997]. A strong correlation between the spatial coverage of microscale breaking and gas transfer velocity has been demonstrated by *Zappa* [1999] and *Zappa et al.* [2001], thus supporting the theoretical model of *Csanady* [1990]. Using a combination of IR imagery and particle imaging velocimetry, *Siddiqui et al.* [2001] have shown that regions of high vorticity just behind microbreaker crests can account quantitatively for enhanced gas transfer rates. Finally, *Zappa et al.* [2002] have demonstrated that substantial increases in mean square slope are associated with the microbreaking process. The ubiquitous occurrence of small-scale microbreaking waves in low and moderate wind conditions and their abundance relative to large breaking waves producing whitecaps [*Katsaros and Attaturk*, 1992; *Peirson and Banner*, 2003] suggest that these waves play a major role in promoting gas transfer. Small-scale waves are implicated in a second key process that promotes surface renewal, the generation of longitudinal eddies. Various models have been put forward showing that interactions of a wind-driven surface shear current with the orbital

motions of gravity-capillary waves [*Coantic*, 1986; *Back and McCready*, 1988] could enhance gas exchange. The latter concept is supported by observations of wind-induced longitudinal eddies in both the laboratory [*Melville et al.*, 1998] and in the field [*Gemmrich and Hasse*, 1992]. These studies suggest that small-scale surface waves promote gas exchange by enhancing near-surface turbulence and provide strong motivation to examine the use of mean square slope calculated over an appropriate wave number range, rather than U_{10} or u^*, to parameterize gas transfer velocity.

[7] The differential response of the TOPEX C-band and Ku-band instruments to changes in small-scale surface roughness has been pointed out by several workers [*Chapron et al.*, 1995; *Bliven et al.*, 1996; *Elfouhaily et al.*, 1996, 1998]. The additional sensitivity to small-scale roughness inherent in a dual-frequency approach was utilized by *Chapron et al.* [1995] to improve understanding of surface scattering using a two-scale Kirchoff scattering model. *Elfouhaily et al.* [1998] demonstrated the utility of a differenced mean square slope estimate in improving estimates of local wind stress. They concluded that wind stress estimates using either Ku-band or C-band cross sections were significantly contaminated by residual sea state, including nonlocal effects such as swell. They also concluded that variations in the differenced normalized cross section ($\sigma_0^{\mathrm{C}} - \sigma_0^{\mathrm{Ku}}$) and the differenced mean square slope $\Delta\langle s^2\rangle$ were directly related to changes in the shortest wave scales ($\lambda = 2-16$ cm) due to local wind perturbations and therefore offered a more accurate assessment of wind stress. We extend this argument, suggesting that the differenced altimeter mean square slope estimate, representing small-scale roughness, can be scaled to gas transfer velocity, which correlates closely with the small-scale wave slope. Further, the scaling can be calibrated using wave number slope spectra measured in situ to compute a wave number-windowed estimate of the mean square slope that matches the integrated slope domain relevant to the altimeter.

3. Methodology

[8] A useful measure of the roughness of a water surface with wind-driven waves is the mean square surface slope, defined as

$$\langle s^2\rangle = \int_0^\infty S(\kappa)\kappa d\kappa \tag{1}$$

where $S(\kappa)$ is the omnidirectional, one-sided wave number slope spectrum and κ is the wave number [*Hara et al.*, 1998].

[9] While the total mean square slope is obtained by integrating over all wave numbers ($0 < \kappa < \infty$), it is useful to consider only the mean square slope contribution of waves within a specific wave number range by integrating (1) over the limits $\kappa_1 \rightarrow \kappa_2$, where κ_1 and κ_2 bracket a range of wave numbers contributing strongly to gas transfer. We will designate the result of this definite integral of (1) as $\langle s^2\rangle_{\kappa_1}^{\kappa_2}$. As explained below, wave numbers κ_1 and κ_2 can be chosen to correspond to the upper wave number limits that satisfy the quasispecular scattering condition of the geometrical optics model for the two radar wavelengths used on the TOPEX and Jason-1 altimeters. Thus defined, $\langle s^2\rangle_{\kappa_1}^{\kappa^2}$ can then be compared with the difference in mean square slope estimates derived from Ku-band and C-band backscatter.

3.1. Estimation of Mean Square Slope From Altimeter Backscatter

[10] Mean square slope can be estimated from nadir-looking altimeters using a geometric optics (specular) scattering model [*Brown*, 1990; *Jackson et al.*, 1992]. The mean square slope of waves in the wave number range that satisfies specular scattering conditions is inversely related to the normalized backscatter. *Jackson et al.* [1992] reviewed the application of altimeter normalized backscatter (σ_0) to the estimation of mean square slope. Approximating the surface wavefield as an isotropic Gaussian surface [*Cox and Munk*, 1954], the geometrical optics (GO) form of the integrated microwave backscatter cross section of the wavy surface can be expressed as

$$\sigma_0^{\mathrm{GO}} = \left(\rho_{\mathrm{g}} \sec^4\theta/\langle s_{\mathrm{g}}^2\rangle\right) \mathrm{e}^{\left(-\tan^2\theta/\langle s_{\mathrm{g}}^2\rangle\right)} \tag{2}$$

where ρ_{g} is an effective reflectivity, $\langle s_{\mathrm{g}}^2\rangle$ is an effective mean square slope estimate and θ is the pulse illumination incidence angle. The form (2) neglects anisotropy of the ocean surface with respect to slope [*Liu et al.*, 2000]; however, *Jackson et al.* [1992] conclude, on the basis of several remote sensing data sets at microwave frequencies, that adoption of the isotropic form of the integrated cross section leads at most to an error of a few percent in the estimation of mean square slope. As pointed out by *Jackson et al.* [1992], $\langle s_{\mathrm{g}}^2\rangle$ can be evaluated for aircraft data using a gross fit of the azimuthally integrated cross section shape over a finite angular range. For satellite altimeter observations (near-nadir), it must be determined from the magnitude of the cross section at a fixed incidence angle. In that case, (2) reduces to give mean square slope as

$$\langle s_{\mathrm{n}}^2\rangle = \rho_{\mathrm{n}}'/\sigma_0 \tag{3}$$

where the subscript n is used to indicate nadir ($\theta = 0°$) and ρ_{n}' is understood to differ from a pure Fresnel reflectivity coefficient in that it may include diffraction effects.

[11] In the geometric optics model, the integrated cross section is treated as an incoherent addition of radiation quasispecularly scattered by all wave facets with dimensions greater than a cutoff wavelength $\lambda_{\mathrm{cutoff}} \approx 3\lambda_{\mathrm{i}}$ where λ_{i} is the incident wavelength [*Brown*, 1990; *Elfouhaily et al.*, 1997]. For the TOPEX and Jason-1 Ku-band ($\lambda_{\mathrm{i}} = 2.1$ cm) and C-band ($\lambda_{\mathrm{i}} = 5.5$ cm) channels, these cutoff wavelengths are roughly 6.3 cm and 16.5 cm, respectively. The corresponding cutoff wave numbers are $\kappa_{\mathrm{cutoff}}^{\mathrm{C}} = 40$ rad m^{-1} and $\kappa_{\mathrm{cutoff}}^{\mathrm{Ku}} = 100$ rad m^{-1}. The effective mean square slope variable $\langle s_{\mathrm{n}}^2\rangle$ estimated from either σ_0^{C} or σ_0^{Ku} differs from the total mean square slope as measured by optical methods [e.g., *Cox and Munk*, 1954] in that it represents an integration of the wave number slope spectrum (1) only up to $\kappa_{\mathrm{cutoff}}^{\mathrm{C}}$ or $\kappa_{\mathrm{cutoff}}^{\mathrm{Ku}}$, respectively. The availability of both Ku and C frequency bands on TOPEX and Jason-1 allows isolation of the mean square slope contribution of the small-scale waves between 40 and 100 rad m^{-1} by differencing

the estimates from the two frequency bands. The gas transfer velocity is poorly correlated with mean square slope for wave numbers $\kappa < 25$ rad m^{-1}, but is increasingly well-correlated with mean square slope for higher wave numbers ($\kappa > 40$ rad m^{-1}), suggesting that the direct gas exchange contribution of the small-scale waves is dominant [*Bock et al.*, 1999; *Frew et al.*, 2004]. For the purpose of maximizing the sensitivity and dynamic range of an algorithm for gas transfer velocity k, a reasonable approach is to eliminate slope contributions from the longer waves by assuming that $k \propto \Delta\langle s_n^2\rangle$, where

$$\Delta\langle s_n^2\rangle = \langle s_n^2\rangle^{Ku} - \langle s_n^2\rangle^{C} = \frac{\rho_n'^{Ku}}{\sigma_0^{Ku}} - \frac{\rho_n'^{C}}{(\sigma_0^{C} + \alpha)}, \quad (4)$$

which corresponds to the mean square slope over the approximate wave number range $40 \le \kappa \le 100$ rad m^{-1}. Here α is an ad hoc adjustment to the C-band σ_0 [*Chapron et al.*, 1995] to allow for the fact that there is no absolute calibration of the C-band backscatter cross section for either the TOPEX or Jason-1 instruments. It is worth noting that antenna footprint sizes for both Ku-band and C-band altimeter frequencies are pulse-limited and depend only on the compressed pulse width and significant wave height. Since the compressed pulse width is 3.125 ns (320 MHz bandwidth) for both Ku band and C band [*Chelton et al.*, 2001], the areas sampled by the two radar pulses are identical.

[12] If the relation between k and the mean square slope for the wave number range $\kappa = 40$–100 rad m^{-1} ($\langle s^2\rangle_{40}^{100}$) were known, k could be estimated from the normalized backscatter at the two frequencies, assuming $\Delta\langle s_n^2\rangle \approx \langle s^2\rangle_{40}^{100}$. Such a relation has been determined by *Frew et al.* [2004] from field measurements of wave slope and transfer velocity.

3.2. Gas Transfer Velocity-Mean Square Slope Relation

[13] Currently there are a relatively limited number of laboratory and in situ coincident measurements of k and $\langle s^2\rangle_{40}^{100}$ from which to derive a relation between these two variables. The dependence of k on mean square slope has been determined experimentally [*Hara et al.*, 1995; *Bock et al.*, 1999] in laboratory annular wind-wave tanks of two different scales, a large annular wind-wave facility (diameter = 4 m) at the University of Heidelberg [*Schmundt et al.*, 1995] and a small annular tank (diameter = 0.5 m) at Woods Hole Oceanographic Institution [*Frew*, 1997]. In both studies, gas transfer velocities were estimated using O_2 as a flux tracer and the wave spectrum was modulated by varying both wind speed and surface film concentration. The slope measurement techniques differed for the two tanks. The measurements in the Heidelberg tank were made using a scanning laser slope gauge capable of determining $S(\kappa, \theta, \omega)$ for $\kappa = 30$ to 1200 rad m^{-1}. In the WHOI tank, a fixed-point laser slope gauge was used to measure the frequency slope spectrum. The wave number spectrum was then constructed from the frequency slope spectrum using a dispersion relation [*Bock and Mann*, 1989] and the mean current velocities estimated from fitting peaks in the frequency spectrum corresponding to allowable along-tank wave modes [*Bock et al.*, 1999].

[14] *Bock et al.* [1999] demonstrated a strong correlation between k and mean square slope over the range $\kappa = 50$–1200 rad m^{-1}, with good agreement between the two tanks, particularly for $\kappa > 200$ rad m^{-1}. However, for $\kappa < 200$ rad m^{-1}, they reported significantly higher scatter. We reanalyzed their data over the wave number range $\kappa = 50$–100 rad m^{-1} [*Frew et al.*, 2004], which is close to the range of interest in this work. The reanalysis yielded transfer velocity-mean square slope relationships that differed significantly between the two tanks. For the WHOI and Heidelberg tanks respectively, we obtained, for $Sc = 660$ (the Schmidt number for CO_2 in seawater at 20°C [*Wanninkhof*, 1992]),

$$k_{660}(\text{cm h}^{-1}) = 5.2 + 2.7 \times 10^6 \left(\langle s^2\rangle_{50}^{100}\right)^2 \quad (5)$$

$$k_{660}(\text{cm h}^{-1}) = 4.6 + 5.2 \times 10^5 \left(\langle s^2\rangle_{50}^{100}\right)^2. \quad (6)$$

[15] The substantial discrepancy is likely due to the fact that the wavefields over the wave number range of 50–100 rad m^{-1} were strongly influenced by tank geometry [*Bock et al.* 1999], particularly in the WHOI tank, which had a very small (0.1 m wide × 0.1 m deep) water channel that restricted development of longer waves.

[16] More recently, *Frew et al.* [2004] reported coincident field measurements of k and $\langle s^2\rangle_{40}^{100}$ from the NSF-CoOP Coastal Air-Sea Chemical Fluxes experiment (CoOP-97), conducted from the R/V Oceanus in coastal and offshore waters south of Cape Cod in July, 1997. They measured frequency-wave number slope spectra with a scanning laser slope gauge [*Bock and Hara*, 1995] and estimated gas transfer velocities by scaling heat transfer velocities derived from infrared imagery and heat flux estimates [*Haußecker*, 1996; *Jähne and Haußecker*, 1998; *Schimpf et al.*, 2002, 2004]. The *Frew et al.* [2004] estimate of the k-$\langle s^2\rangle$ relationship for a gas of low solubility at $Sc = 660$ for the wave number range $40 - 100$ rad m^{-1} is

$$k_{660}(\text{cm h}^{-1}) = 1.4 + 7.6 \times 10^5 \left(\langle s^2\rangle_{40}^{100}\right)^2. \quad (7)$$

[17] The laboratory wave tank data were compared with the CoOP97 field data for the wave number range 50–100 rad/m from *Frew et al.* [2004]. The laboratory data sets for this wave number range did not agree very well with each other or with the CoOP97 field data computed for the same wave number range. Since the annular wind-wave tanks used in the laboratory have some limitations in representing oceanic conditions (principally, the suppression of longer waves due to channel depth, the potential for wall effects, the development of secondary flows and the lack of breaking waves), we choose to use the relationship derived from the CoOP97 field observations (7) as the best available estimate of the of k-$\langle s^2\rangle_{40}^{100}$ relationship. We also emphasize that gas transfer velocities in CoOP97 were determined indirectly from thermographic estimates of the ocean skin-bulk temperature difference assuming the surface renewal model, combined with micrometeorological measurements of heat flux. Schmidt number scaling [*Schimpf et al.*, 2004] of the resulting estimated heat transfer velocities was then used to

obtain gas transfer velocities. The use of heat as a proxy for gases and the extrapolation of heat transfer velocities to gas transfer velocities assuming surface renewal is controversial [*Asher et al.*, 2004]. Although, as detailed later in this paper, (7) produces very reasonable k estimates when combined with altimeter slope estimates, we therefore must stress that its universality has yet to be demonstrated.

3.3. Algorithm Description

[18] Using (4) for the Ku-band–C-band mean square slope difference $\Delta\langle s_n^2\rangle \approx \langle s^2\rangle_{40}^{100}$ and assuming the quadratic relation (7) between k and $\langle s^2\rangle_{40}^{100}$ reported by *Frew et al.* [2004], our expression for the Schmidt number-corrected k in cm h^{-1} is

$$k = \left(\frac{Sc(T,S)}{660}\right)^{-0.5} \cdot \left(c_0 + c_1\left(\Delta\langle s_n^2\rangle\right)^2\right), \tag{8}$$

where $Sc(T, S)$ is the Schmidt number of the gas at ambient sea surface temperature T and salinity S [*Wanninkhof*, 1992] and $c_0 = 1.4$ and $c_1 = 7.6 \times 10^5$. The differenced mean square slope $\Delta\langle s_n^2\rangle$ is calculated from (4) using $\rho_n'^{Ku} = 0.427$, $\rho_n'^{C} = 0.617$ and $\alpha = 3.6$; values for these model parameters were determined by an optimization procedure described in section 3.3.3.

[19] We note that by using a Schmidt number exponent $n = -0.5$ in scaling k for a specific gas at the ambient temperature, we slightly overestimate or underestimate k under conditions where winds are low and coherent sea slicks are present since the dependence would trend toward $n = -0.67$ [*Jähne et al.*, 1987]. However, given the weak dependence we expect that, over the normal range of oceanic temperatures, the potential error is small compared with uncertainty in the calibration based on the field data [*Frew et al.*, 2004]. Previous early work [*Jähne et al.*, 1984; *Jähne*, 1985; *Bösinger*, 1986] suggests that the Schmidt number exponent n varies between -0.5 and -0.67 as a smooth function of $\langle s^2\rangle$. Thus it may be possible to refine the Schmidt number dependence in the altimeter algorithm when that functionality is more precisely determined experimentally in the relevant wave number range.

3.3.1. Altimeter Data Sets

[20] The altimeter data sets used for this work were obtained from the California Institute of Technology Jet Propulsion Laboratory (JPL) Physical Oceanography Distributed Active Archive Center (PO.DAAC) in Pasadena, CA and the CNES/CLS Archivage, Validation et Interprétation des données des Satellites Océanographiques (AVISO) in Toulouse, FR. Documentation may be found in the user handbooks for TOPEX and Jason-1 (*Benada* [1997] and *Picot et al.* [2006], respectively). For this work, we have utilized the TOPEX Geophysical Data Record (GDR) (cycles 17–364) and the Jason-1 GDR (cycles 1–21). Additionally, we have applied the GDR Correction Product Version C (GCP-C), released by JPL, to the TOPEX GDRs (ftp://podaac.jpl.nasa.gov/pub/sea_surface_height/topex_poseidon/gcp_c/doc). Now in its third generation, GCP-C incorporates drift corrections to the TOPEX Microwave Radiometer (TMR) 18 GHz brightness temperature [*Ruf*, 2002] as well as long-term calibration adjustments to normalized backscatter (σ_0) as described by *Lockwood et al.* [2005]. Both TOPEX and Jason-1 followed the same nominal ground track with a 254 pass (half orbit), 10-day exact repeat cycle during the period used in this analysis. TOPEX cycles 17–364 cover the period March 1993 to August 2002. This includes the changeover from the failing TOPEX Side-A altimeter to the redundant Side-B altimeter during cycle 234 in February 1999. Jason-1 cycles 1–21 cover the period January 2002 to August 2002 and thus include data from the entire collinear phase of the TOPEX-Jason-1 Tandem Mission [*Emery et al.*, 2004], in which both altimeters followed the same orbit, separated in time by 73 s. The corresponding collinear phase TOPEX cycles are 344–364.

3.3.2. Data Editing and Processing

[21] The normalized backscatter coefficients were extracted from the GDRs, along with record date, time, latitude, longitude, wind speed, and various other variables needed to calculate the atmospheric attenuation corrections to the TOPEX backscatter (see Appendix A). Intrinsic data quality flags and range tests [*Benada*, 1997; *Picot et al.*, 2006] were used to eliminate out-of-range measurements and measurements over land and ice.

[22] The algorithm is sensitive to rain events, which introduce significant perturbations in $\Delta\langle s_n^2\rangle$ since radiation at Ku-band frequency is strongly attenuated by high atmospheric moisture while C-band radiation is only slightly attenuated [*McMillan et al.*, 2002]. This results in unrealistically high estimates of $\Delta\langle s_n^2\rangle$ and therefore k. These anomalies are particularly evident in the low-wind regime. Data impacted by rain events were eliminated from both data sets using the rain flag implemented in both the TOPEX GCP-C and the Jason-1 GDR [see *Tournadre and Morland*, 1997]. The potential bias introduced by excluding rain contaminated data is discussed later in section 4.3.5.

[23] A natural cubic spline was applied to the filtered and corrected data to register the data to a common latitude grid of approximately 7 km spacing, which corresponds to the native 1-Hz resolution of the TOPEX and Jason-1 altimeters. The splined data were then temporally and spatially binned into monthly time frames on a 2.5° spatial grid.

[24] Independent land and ice masks were applied to the binned data to ensure that all data were over water. The land mask was generated at 2.5° resolution from a topographic database of 5′ resolution (DBDB5 bathymetry [*Bowles et al.*, 1998]) with the threshold of the mask based on 25% land coverage within a grid cell. Ice masks were generated at 2.5° resolution from the Special Sensor Microwave Imager (SSM/I) monthly ice product (25 km resolution, greater than 15% ice concentration) of the National Snow and Ice Data Center, CIRES, University of Colorado.

[25] The binned, masked 1-Hz data were then used to compute 1-Hz estimates of gas transfer velocity at $Sc = 660$ from (4) and (8). The 1-Hz gas transfer velocities were averaged at each 2.5° grid point over each month. A 12+ year time series by month for TOPEX and a 6-month time series of TOPEX-Jason collocated product have been constructed [see *Glover et al.*, 2007].

[26] Of critical note for this application are the atmospheric attenuation corrections applied to TOPEX σ_0^{Ku} and σ_0^{C} and the bias corrections applied to Jason-1 σ_0^{Ku} and σ_0^{C} in order to match the output of the two altimeters. Atmospheric attenuation corrections to both σ_0^{Ku} and σ_0^{C} were implemented incorrectly in the original TOPEX GDR and the errors were only partially remedied by *Benada* [1997]. The

proper corrections as applied in this work are described in Appendix A.

[27] In order to investigate potential σ_0 biases between the two altimeters, an analysis of the filtered, splined σ_0 data from the entire TOPEX/Jason-1 collinear phase (on the order of 10^7 data records) was performed. Comparison of the means of σ_0 for the two data sets showed significant offsets in both frequency bands. On the basis of these mean offsets, the following (additive) biases were applied to Jason-1 $\sigma_0^{Ku}$and σ_0^{C}, respectively: -2.39 dB and -0.73 dB. We note that these differ from the bias corrections currently suggested by AVISO/PO.DAAC (-2.26 dB (Ku band) and -0.28 dB (C band)) [*Picot et al.*, 2006].

3.3.3. Optimization of Model Parameters for Mean Square Slope

[28] Accurate knowledge of the values of the parameters of $\rho_n'^{Ku}$, $\rho_n'^{C}$ and α is essential for evaluation of (4). Unfortunately literature values for these parameters are either variable, as in the case for $\rho_n'^{Ku}$ and $\rho_n'^{C}$ [*Jackson et al.*, 1992; *Apel*, 1994; *Freilich and Vanhoff*, 2003], or largely unknown, as in the case for α [*Chapron et al.*, 1995]. Further, *Freilich and Vanhoff* [2003] present evidence that the value of $\rho_n'^{Ku}$ (and by extension $\rho_n'^{C}$) varies with the wind speed (U_{10}). Therefore in this study we have sought average, effective values of $\rho_n'^{Ku}$, $\rho_n'^{C}$ and α that lie within the ranges reported in the literature and effect satellite estimates of mean square slope that match those taken in a field study conducted as part of the 1997 NSF-sponsored Coastal Ocean Processes experiment (CoOP-97) [*Frew et al.*, 2004].

[29] In order to obtain estimates for the above parameters, we calibrated their values against field measurements of mean square slope using a nonlinear, goal attainment, optimization technique. The particular method used was ''fgoalattain'', a multiobjective, goal attainment, sequential quadratic programming technique found in the Matlab optimization toolbox, version 2.3 [*MathWorks*, 2000]. Three equally weighted goals were established for this optimization. First, the reduced χ^2 should be as close as possible to the value of one, a standard goal in nonlinear optimization techniques [*Davis*, 1986]. Second, the slope of the Type-II regression [*York et al.*, 2004] between satellite estimates and field measurements of $\langle s^2 \rangle_{40}^{100}$ should be as close as possible to a value of one. This goal ensured that the optimization retained fidelity to the data over the entire range measured, and third, the intercept of this Type-II regression should be as close as possible to zero; that is, the satellite-derived mean square slope should be zero when the field-observed mean square slope is zero. Note that this does not imply that the gas transfer velocity becomes zero, due to the nonzero constant c_0 in equation (8).

[30] The optimization technique employed in this study starts from initial values and tries to drive the result toward target values constrained by upper and lower limits. The initial values were obtained from a crude fit between field and satellite estimates of $\langle s^2 \rangle_{40}^{100}$. *Freilich and Vanhoff* [2003] investigated the variability of $\rho_n'^{Ku}$ as a function of wind speed by combining the TRMM Microwave Imager (TMI) data with the Precipitation Radar (PR) data from the Tropical Rainfall Mapping Mission (TRMM). Their analysis suggested that the effective reflectivity for the Ku band can vary by as much as 25% over the range of wind speed conditions investigated (0–25 m/s). Theoretical values from *Apel* [1994] were adopted as target values for these parameters and then constrained by allowing them to vary only over the range of values seen in *Freilich and Vanhoff* [2003]. The C-band constraints were arrived at by scaling the Ku-band values with a simple average ratio of $\sigma_0^{C}/\sigma_0^{Ku}$. Given no a priori information as to what the value of the ad hoc C-band calibration coefficient α should be, a generous range of values was allowed to be explored by the optimization software (-8 to $+12$ dB).

[31] Given the mismatch in speed between the two observation platforms (ship *vs.* satellite) and the fact that the field data are neither global nor annual in coverage, concessions were made to extract the maximum amount of information from the combined (ship and satellite) data set, without biasing the optimized parameter results. In the remainder of this section we will provide sufficient detail of these concessions to allow verification.

[32] Field measurements of mean square slopes were made during July 1997 [*Frew et al.*, 2004] in the northwestern North Atlantic using a scanning laser slope gauge [*Bock and Hara*, 1995]. The slope spectral measurements were integrated from 40 to 100 rad m^{-1} to match the portion of wave number space sampled by the dual frequency altimeter onboard TOPEX. The satellite ground track data were subsampled to lie within the geographic and temporal extent of the CoOP-97 field campaign. Owing to the nature of the TOPEX orbit, this subsampling yielded too few data for a robust optimization. Careful examination of the distributions of wind speeds in July for the years 1996, 1997 and 1998 within the CoOP97 study area led us to conclude that there is no statistically significant difference between the means of the U_{10} distributions for these three years at the 95% confidence level. Similarly, we looked at the corresponding distributions of the TOPEX σ_0 values (Ku band and C band) and found that they were statistically indistinguishable. Consequently, the same geographic area was also subsampled from TOPEX July 1996 and 1998 data in order to increase the number of data points in each wind speed bin for the optimization. While not coincident with the field observations, these data represent a regional sampling of ocean surface conditions for July.

[33] Wind speed at 10 m height (U_{10}) was used as an index of convenience to align the field and satellite measurements. The U_{10} field measurements were taken from a shipboard meteorological package [*Edson et al.*, 1998] and adjusted to a neutrally stable 10 m height above the air-sea interface. The satellite estimates of U_{10} [*Gourrion et al.*, 2002] were obtained from the GDR Correction Product, version C (GCP-C). In order to remove any bias in the TOPEX-based U_{10}, the satellite winds were corrected using a linear relationship (Type-I) derived from an updated version of *Gommenginger et al.* [2002] matched buoy-satellite wind speed database. The aligned data were then grouped in variably sized wind speed bins prior to optimization. By adjusting the size of the U_{10} bins (ΔU_{10}) chosen a priori, an additional, unconstrained control was placed on the optimization; larger bins yielded smoother data, but fewer optimization points and vice versa.

[34] The presence of sea surface films of biological origin [*Frew*, 1997; *Frew and Nelson*, 1999; *Frew et al.*, 2002] complicates a comparison of field and satellite mean square

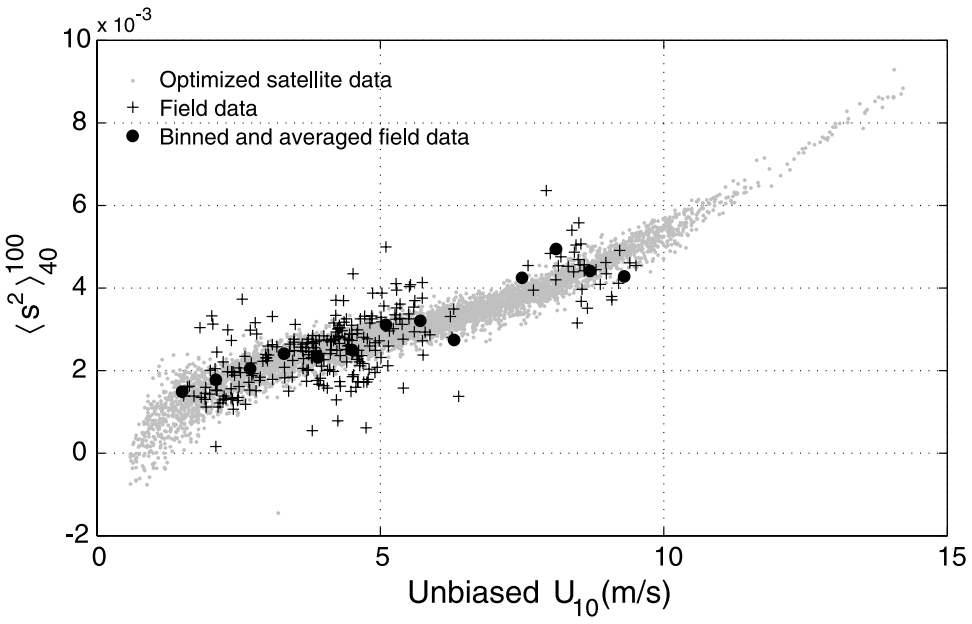

Figure 1. Field estimates (July, 1997) of mean square slope $\langle s^2 \rangle_{40}^{100}$ (pluses), bin-averaged $\langle s^2 \rangle_{40}^{100}$ (black dots) and optimized satellite estimates (July 1996, 1997, 1998) of $\Delta \langle s_n^2 \rangle$ (gray dots) plotted versus unbiased wind speed (U_{10}) within the CoOP97 study area [*Frew et al.*, 2004]. Bias in the satellite estimates of U_{10} was removed through a comparison of the TOPEX-NBDC observation matchups in the *Gommenginger et al.* [2002] data set. See Table 1 for optimization parameters.

slope estimates when indexed by wind speed. The well-known attenuation of surface roughness by surface films [*Cox and Munk*, 1954] skews altimeter U_{10} estimates toward lower values relative to ground-based measurements. The CoOP-97 study area covered a wide range of biological productivity levels and surface conditions at low to moderate wind speeds. Film coverage ranged from undetectable to heavily slicked conditions [*Frew et al.*, 2004]. Collocated measurements of mean square slope and surface chemical enrichments of colored organic matter (CDOM) fluorescence, which acts as a proxy for the presence of surface films [*Frew and Nelson*, 1999; *Frew et al.*, 2002], allowed assessment of potential surface film influences on small-scale wave characteristics [*Frew et al.*, 2004]. By using the excess CDOM at the air-sea interface with respect to the bulk water concentration (δCDOM), samples contaminated by surface films were excluded from the optimization. This further, a priori constraint operates in the opposite sense of ΔU_{10}, the larger δCDOM the more data points used, but the greater the contamination of the optimization data by surface films and vice versa.

4. Results and Discussion

4.1. Optimized Model Parameters

[35] The results of the optimization exercise to match the field and satellite measurements ($\langle s^2 \rangle_{40}^{100}$ and $\Delta \langle s_n^2 \rangle$, respectively) are shown in Figure 1 and Figure 2. In Figure 1, the CoOP97 in situ optical slope gauge estimates [*Frew et al.*, 2004] (1 min averages) of mean square slope, $\langle s^2 \rangle_{40}^{100}$, (crosses) and the bin averaged $\langle s^2 \rangle_{40}^{100}$ (black solid circles) are plotted versus unbiased U_{10}, along with the optimized 1-Hz TOPEX estimates of $\Delta \langle s_n^2 \rangle$ (gray solid points) for the month of July, years 1996–1998. The initial values of the parameters, the lower and upper bounds, optimal values and the χ_v^2 goal obtained are given in Table 1. The values of ΔU_{10} and δCDOM that yielded excellent goal attainment ($\chi_v^2 = 1.$, Type-II slope = 1., and Type-II intercept = 0.) were found to be $\Delta U_{10} = 0.6$ m s^{-1} and $\delta\text{CDOM}_{max} = 0.025$.

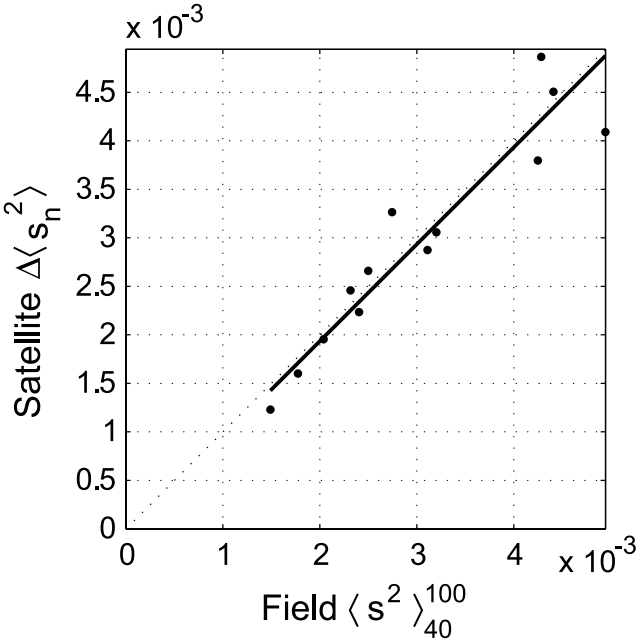

Figure 2. Bin-averaged optimized satellite-derived $\Delta \langle s_n^2 \rangle$ plotted against bin-averaged field $\langle s^2 \rangle_{40}{}^{100}$ measured during CoOP97, showing that the slope (0.9999) and intercept (-6.69×10^{-5}) of the linear regression ($r^2 = 0.8851$, n = 13) closely approach the optimization goals of one and zero, respectively. Bin averaging was performed with $\Delta U_{10} = 0.6$ m s^{-1} and $\delta\text{CDOM}_{max} = 0.025$.

Table 1. Optimization Parameters

	$\rho_n'^{Ku}$	$\rho_n'^{C}$	α	χ^2
Initial value	0.4000	0.5100	1.325	
Lower bound	0.2135	0.2926	−8.0	
Upper bound	0.4685	0.6174	12	
Optimized value	0.4274	0.6174	3.608	0.99993

With these values the optimized parameters were found to be $\rho_n'^{Ku} = 0.427$, $\rho_n'^{C} = 0.617$, and $\alpha = 3.6$. Of these optimal parameters, only the value for $\rho_n'^{C}$ was on the edge of a region of maximum allowed (constrained) value. Figure 2 shows the Type-II regression between field and satellite estimates of $\langle s^2\rangle_{40}^{100}$ and $\Delta\langle s_n^2\rangle$. It is apparent from Figures 1 and 2 that the differenced mean square slopes $\Delta\langle s_n^2\rangle$ are consistent with in situ optical estimates of mean square slope over the same nominal wave number range ($\langle s^2\rangle_{40}^{100}$) using the optimized effective reflectivities. These reflectivities are in reasonable agreement with previously reported literature values. *Jackson et al.* [1992] arrived at values of $\rho_n'^{Ku}$ ranging from 0.38 to 0.52, based on fits of model wind speed algorithms to various aircraft and satellite altimeter data sets. *Apel* [1994] found $\rho_n'^{Ku} = 0.34$ from fits of vertical incidence Ku-band cross sections to ocean data obtained from aircraft and spacecraft. *Vandemark et al.* [1997] also used $\rho_n'^{Ku} = 0.34$ in their analysis of mean square slope data from the aircraft-mounted Radar Ocean Wave Spectrometer (ROWS) altimeter to produce wind stress estimates. The estimate of the average $\rho_n'^{Ku} = 0.427$ derived in this analysis thus lies in the middle of the range of literature values.

[36] The effective C-band reflectivity is expected to be somewhat larger than the Ku-band coefficient since the reflectivity decreases monotonically with increasing frequency [*Apel*, 1994] and the effectively filtered sea surface appears smoother at lower frequencies. The pure (theoretical) Ku-band and C-band Fresnel reflectivities are 0.62 and 0.65 respectively [*Apel*, 1994]. *Apel* [1994] found $\rho_n'^{C} = 0.46$ based on a modeled surface wave vector spectrum, while *Elfouhaily et al.* [1997] suggested $\rho_n'^{C} = 0.61$, which is close to value of 0.617 found in this study.

[37] *Chapron et al.* [1995] suggest an ad hoc TOPEX σ_0^C correction of -1 dB based on an analysis of the relative response of the Ku-band and C-band channels using an empirical model of the sea spectrum. However in later work using σ_0^{Ku} and σ_0^C to estimate wind stress [*Elfouhaily et al.*, 1997], the only corrections applied to σ_0^C are those for atmospheric attenuation by water vapor. We found it necessary to implement this ad hoc correction in our algorithm to properly match satellite and field estimates of mean square slope. The optimum value of this ad hoc C-band correction (α) was found to be 3.61. We note that this applies to the TOPEX Side A altimeter only. *Glover et al.* [2007] have determined the value of α applicable to TOPEX Side B data (designated α_B to distinguish it from α_A for TOPEX Side A) by means of a time series analysis of data spanning the Side A to Side B transition. They found that a slightly larger ad hoc correction ($\alpha_B = 3.72$) was required to compensate for offset between the two TOPEX altimeters.

[38] At this point all of the information pertaining to the optimal values of these three parameters has been used. Any improved optimization awaits more field data collocated in space and time with Jason-1 overflights.

4.2. Differenced Ku-Band and C-Band Mean Square Slope Estimates

[39] Normalized backscatter ($\sigma_0^{Ku}$and σ_0^C), mean square slopes ($\langle s_n^2\rangle^{Ku}$ and $\langle s_n^2\rangle^C$) derived from Ku-band and C-band backscatter, respectively, and the differenced mean square slope ($\Delta\langle s_n^2\rangle$) are shown in Figure 3 as a function of latitude for TOPEX cycle 313, pass 008 (13 March 2001). Pass 008 (ascending) traverses the Pacific Ocean from 66 °S to 50 °N and thus presents a wide range of ocean conditions. In Figure 4a, Ku-band and C-band mean square slope estimates are shown as a function of TOPEX U_{10} for a compilation of all Pass 008 measurements for the year 1995 (data set decimated for clarity). The differenced mean square slope is shown for the same data subset in Figure 4b. These examples illustrate the relatively limited dynamic

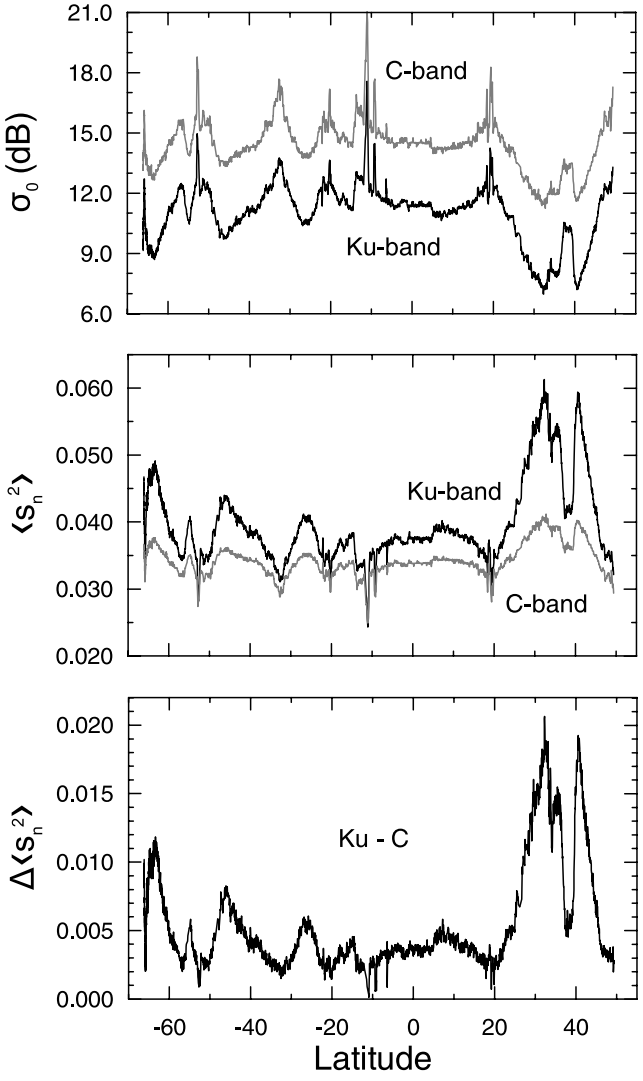

Figure 3. Variation of (top) σ_0^{Ku} and σ_0^C, (middle) $\langle s_n^2\rangle^{Ku}$ and $\Delta\langle s_n^2\rangle^C$, and (bottom) $\Delta\langle s_n^2\rangle$ with latitude for TOPEX Pass 008, Cycle 313, which traverses the Pacific Ocean from 66°S to 50°N and thus represents a wide range of ocean conditions.

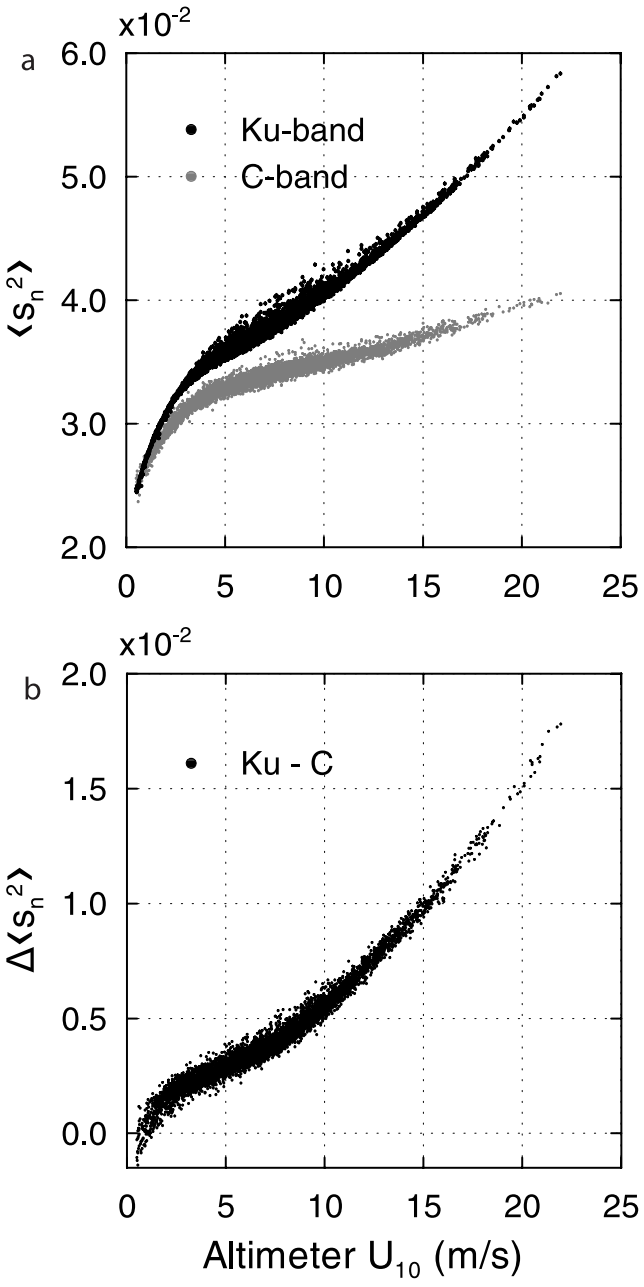

Figure 4. Variation of (a) $\langle s_n^2 \rangle^{Ku}$ and $\langle s_n^2 \rangle^{C}$ and (b) $\Delta\langle s_n^2 \rangle$ with altimeter U_{10} for Pass 008 observations during 1995, illustrating the much larger dynamic range achieved by differencing the Ku-band and C-band mean square slope estimates.

range (a factor of 2–3) observed for mean square slope calculated from either frequency band alone. Initial attempts to calculate air-sea gas transfer velocities from either $\langle s_n^2 \rangle^{Ku}$ or $\langle s_n^2 \rangle^{C}$ yielded transfer velocities that did not span the full range of values typically observed in situ. This is attributable to the fact that the altimeter backscatter includes returns from long waves that contribute to the total mean square slope but do not contribute strongly to gas transfer. The differenced mean square slope (Figures 3 and 4b), however, exhibits a significantly larger dynamic range (>10^2).

[40] In the absence of waves of $\kappa > \kappa_{cutoff}^{C}$, the sea surface should appear equally smooth at either microwave frequency. One of the requirements of the optimization was therefore that $\Delta\langle s_n^2 \rangle$ approach zero for calm, glassy sea conditions. Such conditions are signaled by anomalously high backscatter returns or 'σ_0 blooms' [*Mitchum et al.*, 2004]. Values of σ_0^{Ku}exceeding 16 dB are generally considered to represent specular returns from smooth or glassy seas, based on an analysis of reflected pulse shape and the seasonal and geographical distributions of these high backscatter events [*Mitchum et al.*, 2004]. A somewhat more conservative, albeit arbitrary cutoff ($\sigma_0^{Ku} > 17.5$ dB) was used for filtering the data in this study. A plot of $\Delta\langle s_n^2 \rangle$ as a function of σ_0^{Ku} is shown in Figure 5, illustrating that the mean of $\Delta\langle s_n^2 \rangle$ trends to zero at $\sigma_0^{Ku} = 17.5$dB.

[41] In our optimization procedure, high CDOM, slick-contaminated ship-based observations were eliminated to allow indexing of satellite and ground observations by wind speed. High CDOM ground observations, because they lie anomalously below the main trend of the data in Figure 1 (i.e., very low slope for a given wind), skew the optimization such that the resultant model parameters are outside the range of published values (i.e., physically unrealistic). We examined the potential effect of slick-contaminated satellite observations in the calibration data set, since their influence on the optimization would be passed on to the algorithm in the form of a bias. We performed a Monte Carlo simulation with the calibration data set in which we perturbed a known percentage of randomly selected data points by substituting their values with slick-contaminated values. We used the average σ_0^{Ku} and σ_0^{C} values of all points in the calibration data set for which $\sigma_0^{Ku} \geq 16$ dB as representative values of

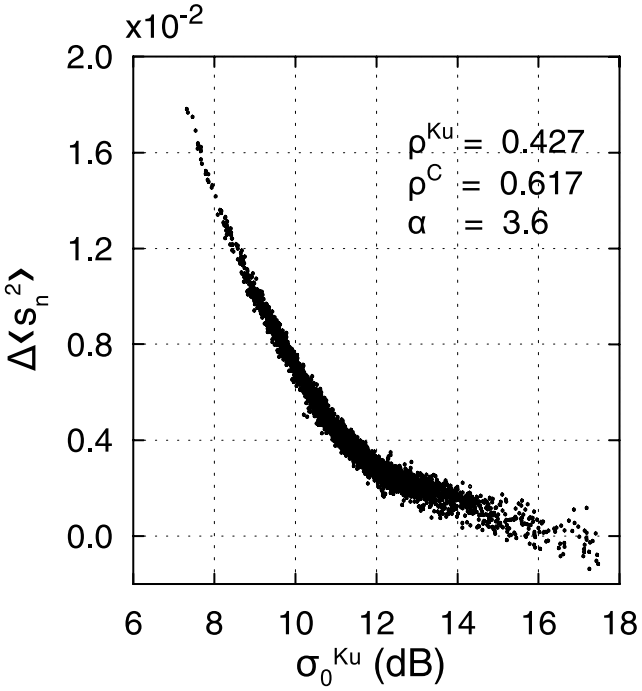

Figure 5. Variation of $\Delta\langle s_n^2 \rangle$ computed from (4) using the optimized parameters with the Ku-band backscatter, σ_0^{Ku}. The differenced slope $\Delta\langle s_n^2 \rangle$ trends to zero at 17.5 dB, the cutoff imposed for valid σ_0^{Ku} values.

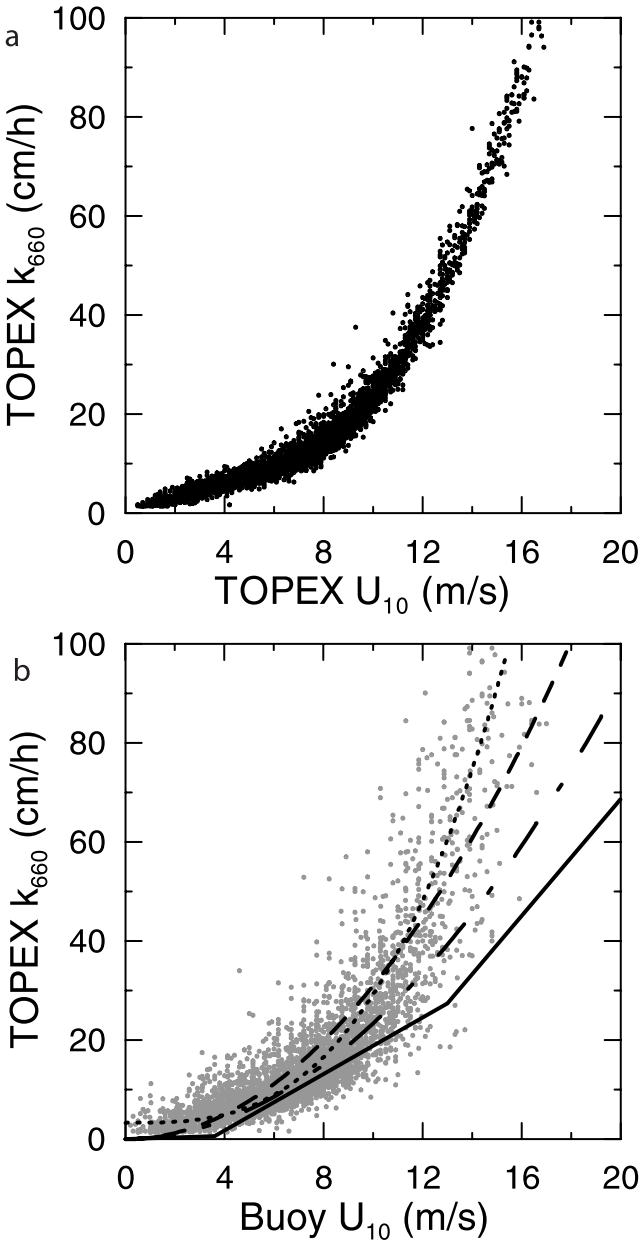

Figure 6. TOPEX k_{660} computed from (8) versus (a) TOPEX U_{10} and (b) collocated buoy U_{10} for the data set compiled by *Gommenginger et al.* [2002] for TOPEX-buoy matchups (∼4350 observations). Observations were considered to be collocated if made within 50 km and 1 hour of each other. Several conventional wind speed-transfer velocity relationships are illustrated for comparison: dashed line, W1992 [*Wanninkhof*, 1992], dotted line, MEA2001 [*McGillis et al.*, 2001a], long-short dashed line, NEA2000 [*Nightingale et al.*, 2000b] and solid line, LM1986 [*Liss and Merlivat*, 1986].

potentially slick-contaminated satellite data in the calibration data set [*Mitchum et al.*, 2004]. Randomly selecting a known percentage of the calibration data points, we changed their σ_0^{Ku} and σ_0^{C} values to these average 'slick' values and then reoptimized the $\langle s^2 \rangle$ parameters used in our algorithm. We repeated this procedure 1000 times for each known percentage and accumulated statistics to evaluate the effect these perturbations had on the gas transfer velocity computed with these perturbed parameters. The known percentage of slicked observations was varied from one to 25% and a RMS difference between the 1000 k and a reference k (calculated using the unperturbed parameters) was calculated. The average effect on mean gas transfer velocities for 1% contamination of the calibration data was to introduce a 0.85% decrease (or bias) in the transfer velocity, while for 5% the bias introduced was 4.2%, and for 10% an 8.4% relative error was introduced. From this exercise we conclude that slick-contaminated data points in the calibration data set have an effect that scales linearly with the prevalence of their occurrence. *Tournadre et al.* [2006] suggest that approximately 5% of Ku-band altimeter observations are characterized by high σ_0^{Ku} on a global basis; these tend to be concentrated in certain geographic regions of climatologically weak winds consistent with slick occurrence [*Mitchum et al.*, 2004]. For our particular calibration data set and data filtering criteria, however, data points with sufficiently high σ_0^{Ku} and σ_0^{C} values to be potentially slick-contaminated after filtering represent a small fraction (approximately 0.4%) of the data considered. Hence their effect on the algorithm was likely small.

4.3. Gas Transfer Velocity Estimates

4.3.1. Comparison With Wind Speed Parameterizations

[42] The TOPEX-derived gas transfer velocities can be compared with estimates from conventional wind speed parameterizations of transfer velocity. Although the altimeter algorithm is not dependent on wind estimates, it is instructive to examine the apparent relationship between transfer velocity and wind speed to illustrate the general characteristics of the algorithm as compared to those in current use. The k_{660}-U_{10} (TOPEX) relationship is well behaved (Figure 6a), as expected, since both variables are derived from σ_0^{Ku}. However, independent, collocated wind estimates are required to compare our algorithm output with results from conventional methods. A compilation of ∼4350 independent observations of wind speed from 41 open water buoys located near TOPEX ground tracks [*Gommenginger et al.*, 2002] was used to make the comparison. The data compilation, kindly provided by C. Gommenginger, National Oceanography Centre, Southampton, U.K., included buoy observations from the National Data Buoy Center (NDBC), the Canadian Marine Environmental Service (CMEDS), the U.K. Meteorological Office (UKMO) and the Japanese Meteorological Agency (JMA). The buoy observations were considered to be collocated with the TOPEX observations if they were positioned within 50 km of the TOPEX ground track and recorded within one hour of the satellite overpass. Figure 6b shows TOPEX-derived k_{660} as a function of buoy U_{10} for the Gommenginger et al. data set. The *Liss and Merlivat* [1986] piecewise-linear relation (LM86), the *Wanninkhof* [1992] quadratic relation (W92), the *Nightingale et al.* [2000b] quadratic relation (NEA00) and the *McGillis et al.* [2001a] cubic relation (MEA01) describing transfer velocity as a function of wind speed are superimposed for comparison. The TOPEX algorithm, calibrated with the CoOP97 data, is seen to produce estimates of k_{660} that are

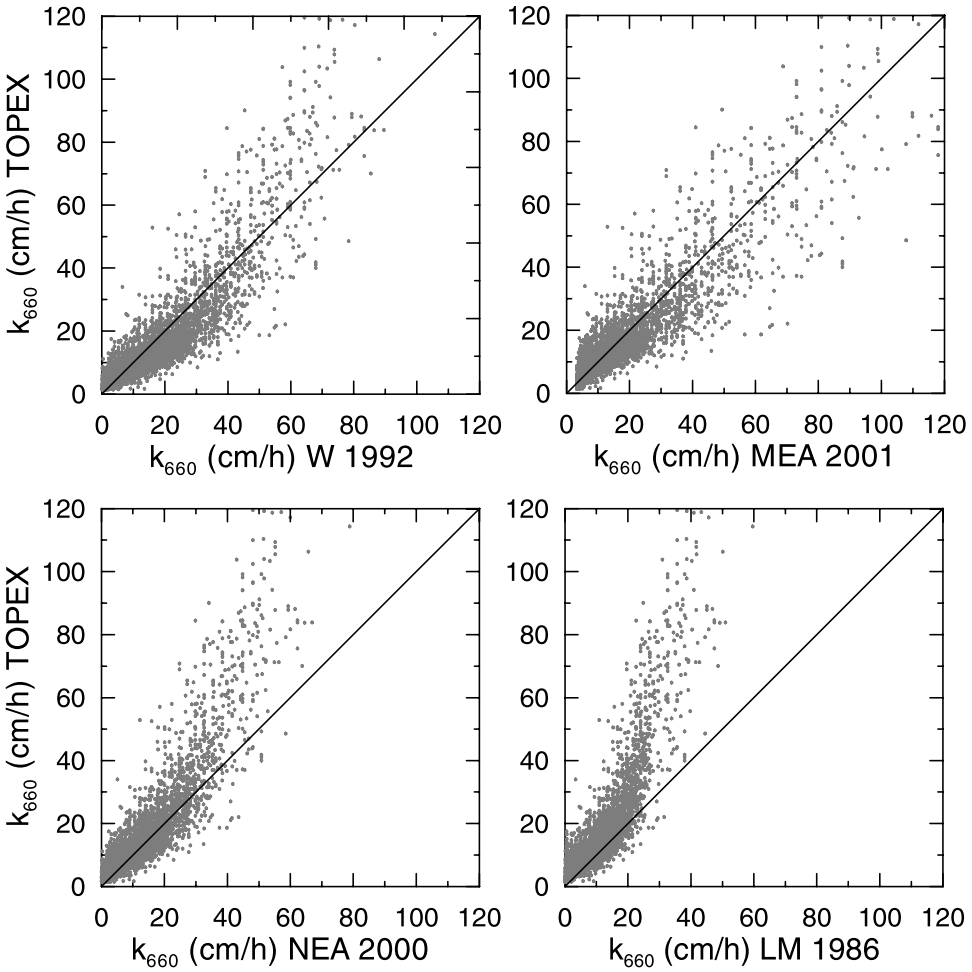

Figure 7. TOPEX k_{660} computed from (8) versus k_{660} computed from four wind speed-transfer velocity relationships (W1992, MEA2001, NEA2000, and LM1986) using collocated TOPEX-buoy observations [*Gommenginger et al.*, 2002].

within the same range as currently accepted algorithms based on wind speed. Differences are illustrated in more detail in Figure 7 by crossplotting TOPEX k_{660} against k_{660} from the same wind speed-transfer velocity relationships. Computed TOPEX transfer velocities tend to be higher than LM86 transfer velocities at all wind speeds. For winds above 12 m s^{-1}, the TOPEX algorithm also generally predicts higher transfer velocities relative to the W92 and NEA00 predictions, but yields results similar to those predicted by MEA01 cubic relationship. In the low-wind regime (U_{10} < 4 m s^{-1}), TOPEX results are seen to be generally in agreement with MEA01 and biased higher than NEA00 and W92, while for 4 $\leq U_{10} \leq$ 12 m s^{-1} range, TOPEX results agree best with NEA00 and MEA01 and are biased low relative to W92.

4.3.2. Comparison and Tentative Validation With Field Measurements

[43] Direct validation of the new algorithm is tentative because of the general lack of field data corresponding in time and space to TOPEX overflights. In this section, algorithm accuracy is assessed using available field measurements from the CoOP97 experiment and from the GasEx-1998 [*McGillis et al.*, 2001a, 2001b] and GasEx-2001 cruises [*McGillis et al.*, 2004].

[44] A check on the internal consistency of the algorithm may be made by comparing the algorithm output for individual satellite overflights within the CoOP97 data set from which the algorithm is derived. Ground estimates of k_{660} during the CoOP97 experiment were based on passive IR estimates of the skin-bulk temperature difference and ship-board heat flux measurements, from which heat transfer velocities were derived and converted to k_{660} using Schmidt number scaling [*Schimpf et al.*, 2004; *Frew et al.*, 2004]. Only four coincident, collocated observations from low-wind conditions are available; these are plotted in Figure 8. Discrepancies between these few altimeter and ground estimates are generally 1 cm h^{-1} or less.

[45] Altimeter k_{660} estimates can be compared with ground observations from the GasEx-1998 and GasEx-2001 air-sea exchange campaigns which took place in the North Atlantic and eastern equatorial Pacific Oceans, respectively. The study areas and cruise tracks for these expeditions are shown in Figure 9 along with sampling points along the altimeter's ground tracks within the cruise

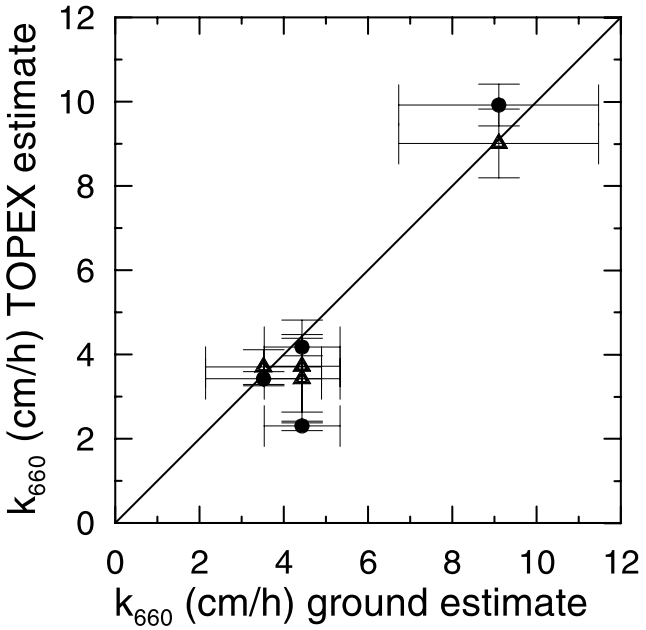

Figure 8. A direct comparison of coincident TOPEX and ground estimates of k_{660} during the CoOP97 gas exchange experiment. Solid circles represent single, 1-s observations over site. Triangles represent average of five consecutive 1-s observations centered over site. A solid 1:1 line is shown for reference.

area. Bin-averaged gas transfer velocities obtained from direct covariance flux estimates during GasEx-1998 have been summarized by *Wanninkhof and McGillis* [1999] and by *McGillis et al.* [2001a, 2001b] and for GasEx-2001 by *McGillis et al.* [2004]. Figure 10 compares TOPEX observations within the study areas during the respective experiment periods with the fitted $U_{10} - k_{660}$ (cubic) relations reported for the bin-averaged k_{660} ground observations [*McGillis et al.*, 2001a, 2004] in each experiment. Collocated, coincident altimeter observations (within 1 hour and 25 km of the GasEx ground tracks) are emphasized using open circles in Figures 9 and 10.

[46] Since the measurement uncertainties for the binned transfer velocities underpinning both of the cubic relations reported by *McGillis et al.* [2001a, 2004] are rather large (order of 60–100%), it is difficult to be very conclusive about the accuracy of the altimeter algorithm; however, the algorithm produces transfer velocities that are within the range of error attributed to ground observations.

[47] Figure 11 summarizes the RMS deviations of the TOPEX-derived k_{660} from the cubic fits in 1 m s^{-1} wind speed bins. The overall average RMS deviation for GasEx-1998 is 3 cm h^{-1}; for coincident, collocated observations only, it is 0.4 cm h^{-1}. The RMS deviations fall in the range 1–2 cm h^{-1} for wind speeds up to 7 ms s^{-1}, increasing significantly at 8 m s^{-1} and above, where the computed TOPEX values begin to fall below the GasEx-1998 cubic fit (see Figure 10a). The overall average RMS deviation for GasEx-2001 is 2.5 cm h^{-1}; for coincident, collocated observations only, it is 1.5 cm h^{-1}. However, in contrast to the GasEx-1998 comparison, the TOPEX observations during GasEx-2001 show the largest deviations (3–6 cm h^{-1}) at low wind speeds, decreasing to 2 cm h^{-1} or less for wind speeds above 4 m s^{-1} wind (see Figure 10b). TOPEX observations produce lower transfer velocities than predicted by the GasEx-2001 cubic $U_{10} - k_{660}$ relation [*McGillis et al.*, 2004]; the latter predicts a substantial gas transfer velocity at $U_{10} = 0$ (8.2 cm h^{-1}). *McGillis et al.* [2004] have suggested that gas transfer velocities were enhanced at low wind speeds during GasEx-2001 owing to strong diurnal stratification and overturning of the shallow mixed layer. Since the TOPEX measurement is based on surface roughness, it is not expected to capture exchange contributions due to buoyancy effects.

[48] Lacking individual point measurements of gas transfer velocity sufficiently located in space and time that are independent of the data set we used to calibrate our algorithm, estimates of the overall uncertainty of the algorithm require opportunistic approaches. We use the closed form relationships between wind speed and gas transfer

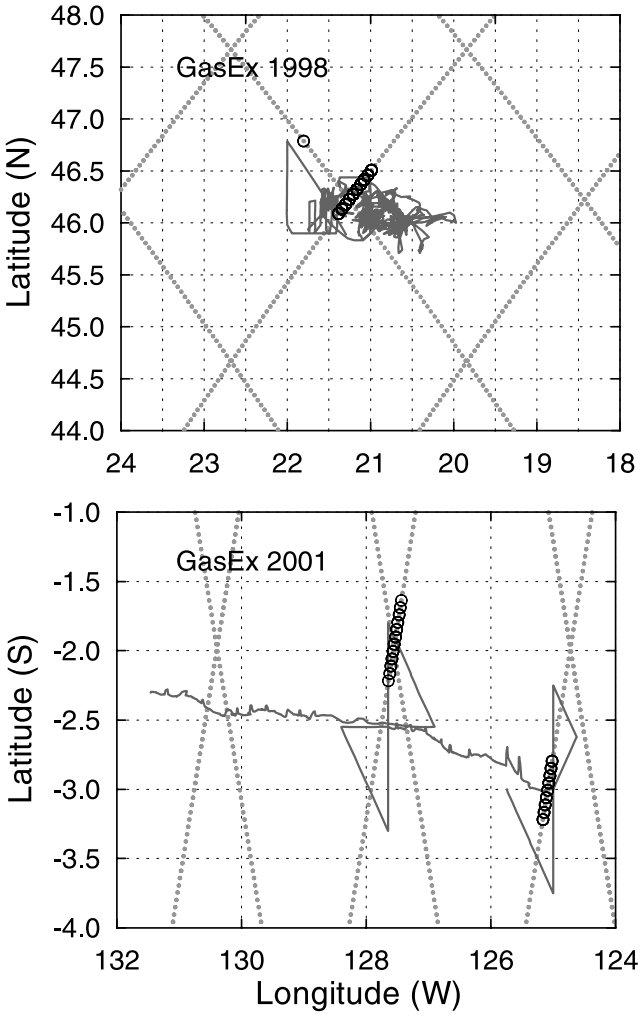

Figure 9. Geographic study areas for (top) the GasEx-1998 experiment in the northern Atlantic Ocean and (bottom) the GasEx-2001 experiment in the eastern equatorial Pacific Ocean. Solid lines represent the ship's tracks; dotted lines represent the TOPEX tracks through the study areas. Open circles indicate collocated observations (within 25 km and 1 hour).

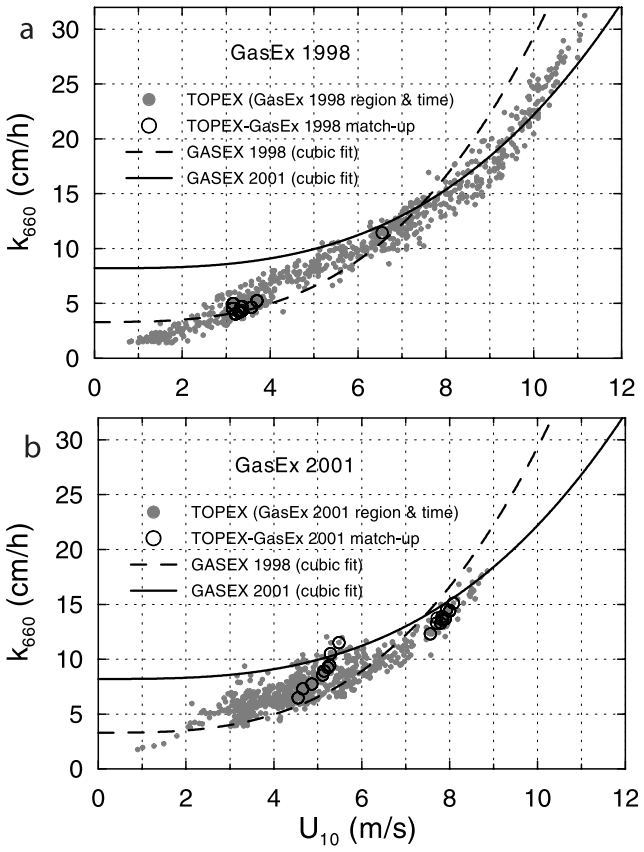

Figure 10. TOPEX estimates of k_{660} within the study areas during (a) GasEx-1998 and (b) GasEx-2001. Open circles represent TOPEX crossovers (collocated with ship track to within 25 km and 1 hour). Cubic best fits to the GasEx-1998 and GasEx-2001 shipboard k_{660} observations, as reported in the work of *McGillis et al.* [2001a, 2004], are shown for comparison.

velocity fit to the GasEx-1998 and GasEx-2001 field data [*McGillis et al.*, 2001a, 2004]. We also extract from the satellite data record all of the data that fall within the overall space and time window of these two field campaigns. Treating the functional forms of these relationships as ground truth, we can evaluate how well our extracted data matches in an ensemble sense. Restricting the comparison to data that was within ±1 hr and 25 km in order to compare only the most relevant satellite estimates, the RMS difference between satellite estimates and the GasEx-1998 relationship is ±8% and with the GasEx-2001 relationship ±11%. We consider these estimates of uncertainty to be optimistic, but are left with the fact that they are comparisons between satellite estimates and independent field measurements averaged into a least squares fit.

[49] A second way to evaluate the algorithm's accuracy is to perform an algorithm parameter perturbation analysis. During optimization of the algorithm parameters as part of the calibration process, the optimization software traversed sizable portions of the possible parameter value subspace. By using these extreme parameter values in the algorithm while calculating the global, area-weighted mean gas transfer velocity we can get an estimate of the algorithm's range. By calculating the long-term RMS difference between these extreme parameter versions of the algorithm and averaging the results, we obtain an uncertainty estimate of ±30%. We assign this more conservative estimate of uncertainty to our value of the long-term, global, area-weighted, Schmidt number corrected, mean gas transfer velocity reported in section 4.3.4.

4.3.3. Measurement Precision of Altimeter Observations

[50] An estimate of the measurement precision of the altimeter observations of k can be made using data from the TOPEX (Side-B)-Jason-1 Tandem Mission, during which the two altimeters followed the same orbit with a slight separation in time. The Jason-1 satellite was launched on 7 December 2001 into the same exact-repeating orbit occupied by the TOPEX/POSEIDON satellite for the previous nine years. The precise placement of the Jason-1 satellite put it 73 seconds (525 km) ahead of TOPEX/POSEIDON probing the same ground track. The first cycle of Jason-1 data collection (15 January 2002) began the calibration/validation or "collinear phase" of the Tandem Mission. This phase lasted until TOPEX/POSEIDON was

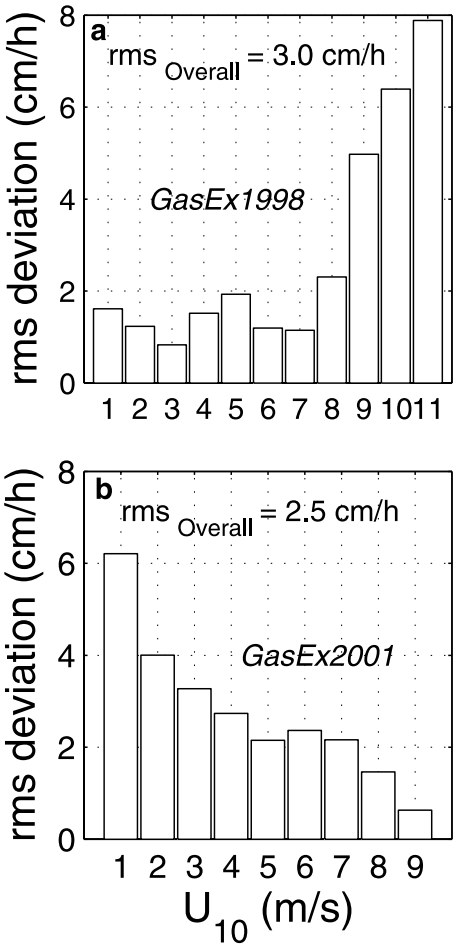

Figure 11. Root mean square deviation of TOPEX k_{660} estimates from k_{660} estimates computed from the cubic U_{10}-k_{660} relations reported for shipboard observations during (a) GasEx-1998 and (b) GasEx-2001 [*McGillis et al.*, 2001a, 2004] in 1 m s^{-1} wind speed bins.

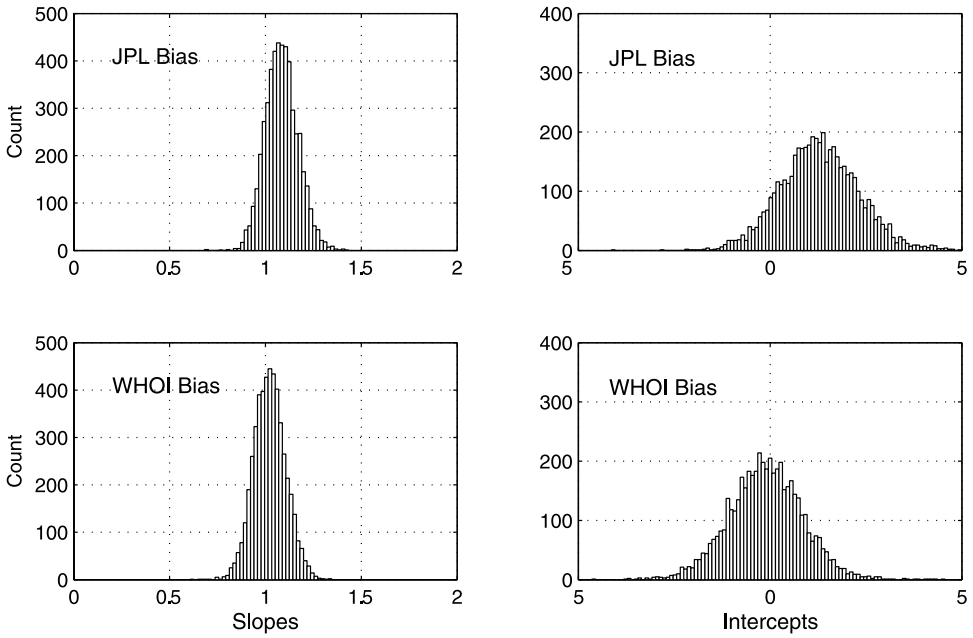

Figure 12. Histograms of slopes and intercepts of regressions of k_{660} (Jason-1) against k_{660} (TOPEX-Side B) computed using the 6.4×10^6 near-coincident, collocated observation pairs recorded during the Tandem Mission collinear phase. Regressions were computed on a pass-bypass basis. (top) Results using JPL $\sigma_0^{Ku}$and σ_0^{C} biases (-2.26 dB and -0.28 dB). (bottom) Results using WHOI $\sigma_0^{Ku}$and σ_0^{C} biases (-2.39 dB and -0.73 dB) determined in this analysis.

moved (11 August 2002) to an orbit in between the orbital tracks of Jason-1 for the start of the ”interleaved phase’. These 21 cycles from the collinear phase (approximately six months) form the basis for intercalibration of the altimeters on the two satellites. Roughly 6.4×10^6 collocated, near-simultaneous observation pairs from the two altimeters are available over the 6-month period.

[51] Our transfer velocity algorithm is sensitive to biases in σ_0. Therefore the along-track Ku- and C-band differences between collocated Jason-1 and TOPEX σ_0 for the entire collinear phase (TOPEX cycles 344–364 and Jason cycles 001–021) were examined. The two instruments should return the same results if their data is processed with the same algorithm; thus a plot of k_{660} (TOPEX) versus k_{660} (Jason-1) should lie along a line with a slope of one and an intercept of zero. Histograms summarizing slopes and intercepts of roughly 5000 pass-by-pass linear fits of k_{660} (Jason-1) versus k_{660} (TOPEX) crossplots computed using all 10^6 collocated σ_0^{Ku} and σ_0^{C} data pairs are shown in Figure 12. The mean slope (1.08) and mean y-intercept (1.29) deviated significantly from the idealized 1:1 line when the recommended AVISO/PO.DAAC additive biases (-2.26 dB (σ_0^{Ku}) and -0.28 dB (σ_0^{C}), *Picot et al.* [2006]) were applied to the Jason-1 data. Our analysis of the collinear phase σ_0 for both frequency bands yielded the following additive biases: -2.39 dB (σ_0^{Ku}) and -0.73 dB (σ_0^{C}). Application of these ‘WHOI’ biases improved the mean slope and the mean intercept for all pass-wise k_{660} (TOPEX) versus k_{660} (Jason-1) linear fits to 1.02 and -0.12 respectively (Figure 12).

[52] Once these biases between TOPEX (Side B) and Jason-1 have been applied, differences in transfer velocity between the two altimeters may derive from two additional sources: random instrument variability and geophysical variability. If one assumes that the variability in the geophysical signal being observed (the radar signal) is stationary on the order of 70 seconds, then variability in transfer velocity produced by the two altimeters with the same algorithm is some measure of the random instrument variability affecting the algorithm. Additionally, high-frequency variability (on the order of 70 seconds or less) in atmospheric and ionospheric corrections factors and similar variability in the sea surface roughness contribute to variance in the transfer velocity even though the same mathematical algorithm is applied. Taken together, these sources of variance in transfer velocity differences between Jason-1 and TOPEX (Side B) are a net estimate of the overall precision of the algorithm.

[53] The RMS precision was estimated by two methods. In the first method, a straightforward Type-II regression analysis [*York et al.*, 2004] of the paired k_{660} values yielded an estimated RMS precision of 7%. The second method employed principal component analysis [*Davis*, 1986]. Following a rotation of axes from data space (k_{660}) to principal component space (principal component scores), the RMS of the second (orthogonal) principal component was taken as a measure of the RMS deviation from an ideal 1:1 relationship between the two variables involved, in this case, Jason-1 k_{660} and TOPEX k_{660}. This analysis yielded an estimated RMS precision of 5%.

[54] The bias-adjusted Jason-1 σ_0^{Ku} and σ_0^{C} values yielded an average global transfer velocity difference of about $+0.9$ cm h^{-1} relative to TOPEX (Side B) during the entire collinear phase based on all observations collectively. An

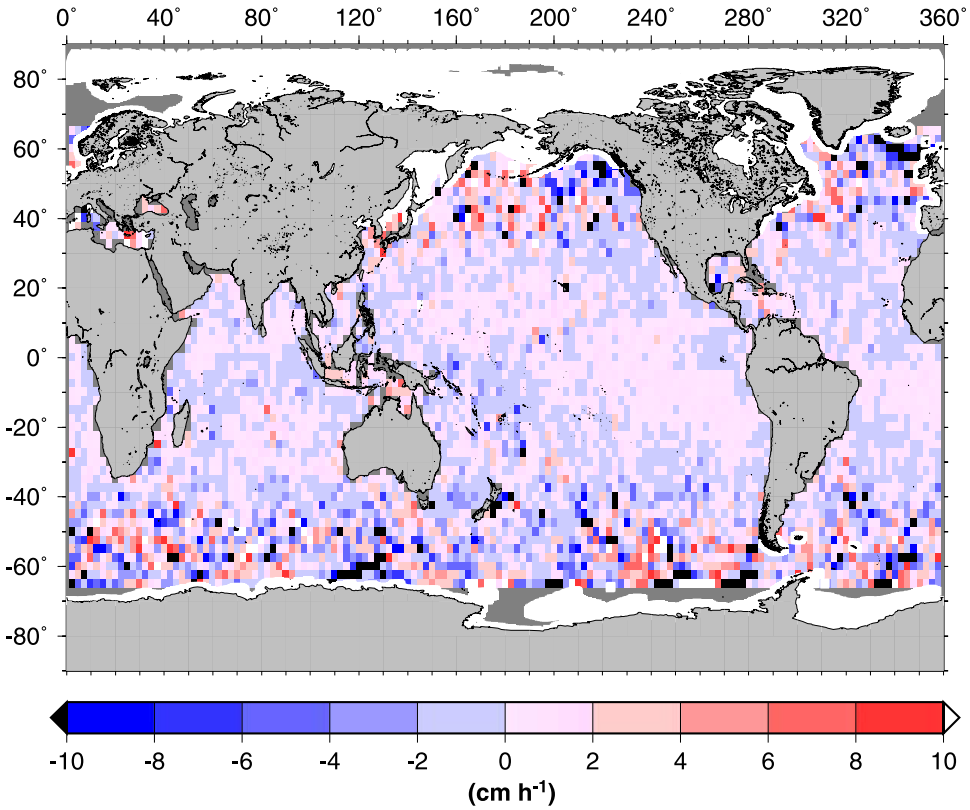

Figure 13. Global map of the average difference between k_{660} (Jason-1) and k_{660} (TOPEX-Side B) for the month of February 2002. The average global transfer velocity difference for the entire Tandem Mission collinear phase is +0.9 cm h^{-1}.

overall bias of +4% in the Jason-1 results relative to the TOPEX results has been determined by Type-II regression analysis as reported by *Glover et al.* [2007].

[55] Figure 13 is a global map of Jason-1−TOPEX (Side B) differences in k_{660} for the month of February 2002. Transfer velocity differences are generally 2 cm h^{-1} or less; however, larger differences (up to 10 cm h^{-1}) are observed. These larger discrepancies are not uniformly distributed, being more prevalent in high-latitude regions. They may arise from short-term (order of 1 minute) variations in wind speed and surface roughness at these latitudes; however they could also be due to processing artifacts in the current version of the Jason-1 GDR, which should be reduced through future reprocessing efforts.

4.3.4. Monthly Global Transfer Velocity Fields

[56] Global, average monthly gas transfer velocity fields for the entire TOPEX record have been generated using the TOPEX GDR/GPC-C data and the new backscatter-based algorithm. The average transfer velocity maps (2.5° × 2.5° grid) for January and July 2003, representing seasonal extremes in both hemispheres, are presented as examples in Figures 14 (top). Figure 14 also shows the TOPEX-derived climatological January and July maps (Figure 14, bottom) computed for the period March 1993 to February 2005. The climatological maps have been smoothed using bilinear interpolation and resampled at 0.5° resolution. The highest monthly average transfer velocities are observed in the north Atlantic and Pacific basins during Northern Hemisphere wintertime, reaching values as high as 75−85 cm h^{-1}. High transfer velocities are similarly observed in the Southern Ocean, particularly in the Indian Ocean sector, during austral winter. Large areas of relatively low transfer velocities (<7 cm h^{-1}) develop in the tropical and equatorial regions, especially at basin margins. The strong effects of the monsoon cycle in the Arabian Sea are evident from a comparison of the July and January maps.

[57] A more detailed view of the seasonal variation is shown in Figure 15, which depicts k_{660} averaged on a zonal basis for the Pacific, Atlantic and Indian Ocean basins and for the global ocean over the 2003 annual cycle. Seasonal variation is highest in the northern Atlantic Ocean, with strong but somewhat weaker variation in the northern Pacific. Variation in the northern Indian Ocean is dominated by the northeast-southwest monsoon cycle in the Arabian Sea and Bay of Bengal. Strong seasonal variation also occurs in the southern ocean, being largest in the Indian and Pacific sectors. An interesting Northern-Southern Hemisphere asymmetry is evident in the summertime development of low transfer velocity regions at midlatitudes (20°N−45°N); these are not observed in the Southern Hemisphere during austral summer.

[58] A more extensive discussion of the 12-year time series of global transfer velocity fields derived from TOPEX is given by *Glover et al.* [2007]. The monthly images and data are available at http://remotesensing.whoi.edu/~david/ktrans/img_dat.html. The overall global average gas transfer velocity at $Sc = 660$ computed for the 12-year time series is 16 ± 4.8 cm h^{-1} [*Glover et al.*, 2007]. Transfer velocity

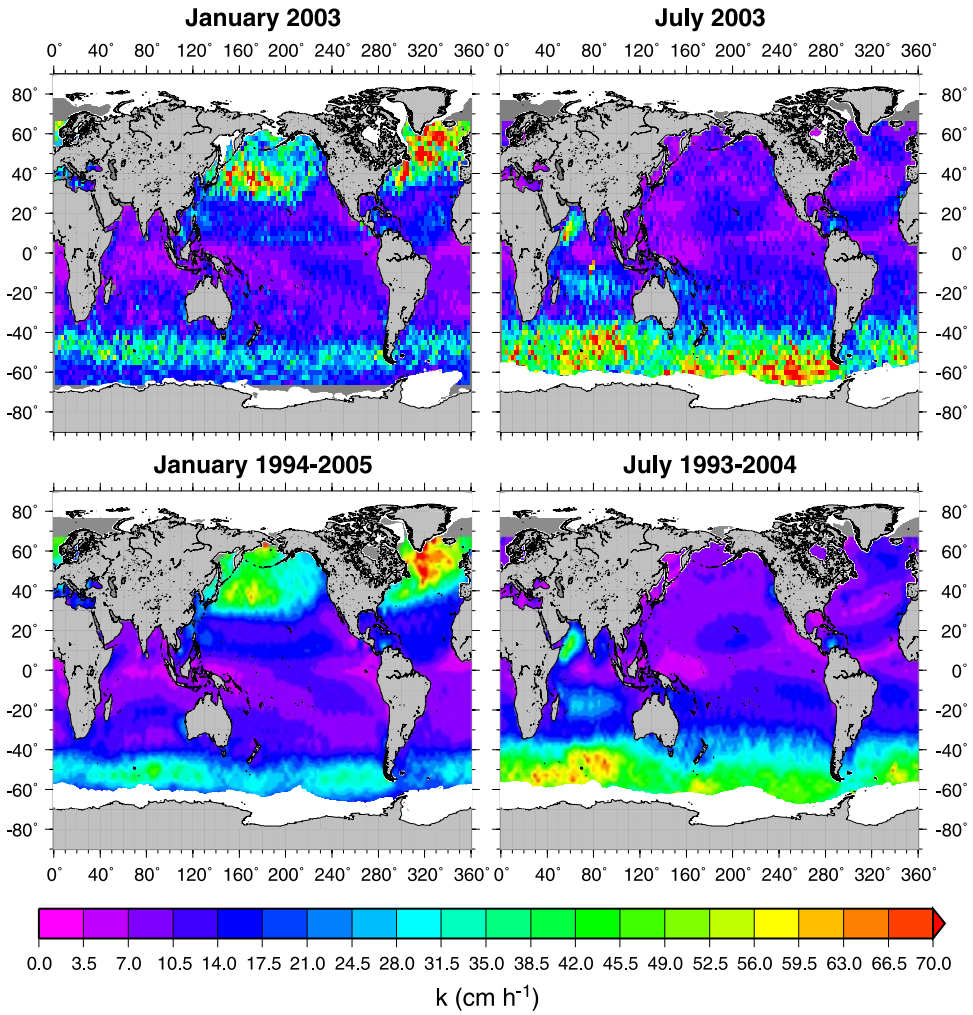

Figure 14. (top) TOPEX-derived average transfer velocity maps (2.5° resolution) for January and July 2003. (bottom) TOPEX-derived climatological January and July maps (0.5° resolution) computed for the period March 1993 to February 2005.

values reported here assume $Sc = 660$ and must be corrected for temperature and salinity dependence [*Wanninkhof*, 1992] using the ambient spatiotemporally varying sea surface temperature and salinity fields. The ambient sea surface temperature has a strong moderating effect on k. Over the normal range of oceanic temperatures, the transfer velocity can vary by more than a factor of two. Since the spatiotemporal distribution of high and low winds also corresponds broadly to regions of cold and warm water respectively, temperature exerts a leveling effect on the transfer velocity and shifts the latitudinal regions of maximum transfer velocity toward the equator relative to maxima in regional winds. Adjusted for the Schmidt number variation with temperature and salinity, our global average k is 13.7 ± 4.1 cm h^{-1}. The adjusted average transfer velocity is derived from model simulations incorporating our altimeter-derived time series into the NCAR Community Climate System Model-Parallel Ocean Program (CCSM3.0-POP) to provide the time-varying temperature and salinity fields [*Moore et al.*, 2004]. Estimates of global average transfer velocity have been revised significantly downward since the original estimates (21.2 ± 5 cm h^{-1} and 21.9 ± 3.3 cm h^{-1} at $Sc = 660$) given by *Wanninkhof* [1992], which were based on natural and bomb ^{14}C ocean inventories, respectively, as estimated by *Broecker et al.* [1986]. *Nightingale et al.* [2000b], using a compilation of dual tracer data from small-scale studies, estimated the global average k at $Sc = 600$ to be 18 cm h^{-1} (k_{660} = 17.2 cm h^{-1}) assuming a Raleigh distribution of winds and 17 cm h^{-1} (k_{660} = 16.2 cm h^{-1}) using one year of ERS-1 scatterometer winds. *Wanninkhof et al.* [2002] estimated the global average to be 17 cm h^{-1} and 18 cm h^{-1}, using cubic and quadratic wind speed dependencies on the NCEP reanalysis winds, respectively. *Naegler et al.* [2006], using updated estimates of the ocean bomb ^{14}C inventory to constrain air-sea CO_2 exchange, estimated the Schmidt number adjusted global average k to be 16.7 ± 2.9 cm h^{-1}. Most recently, further improvements to the bomb-produced ocean inventory of dissolved inorganic radiocarbon and the use of ocean general circulation models in inverse mode to better account for spatiotemporal variations of surface $p^{14}CO_2$ by *Sweeney et al.* [2007] have resulted in a new estimate of 14.6 ± 4.7 cm h^{-1}. Our Schmidt number adjusted global average k (13.7 ± 4.1 cm h^{-1}), while at the low end of these most

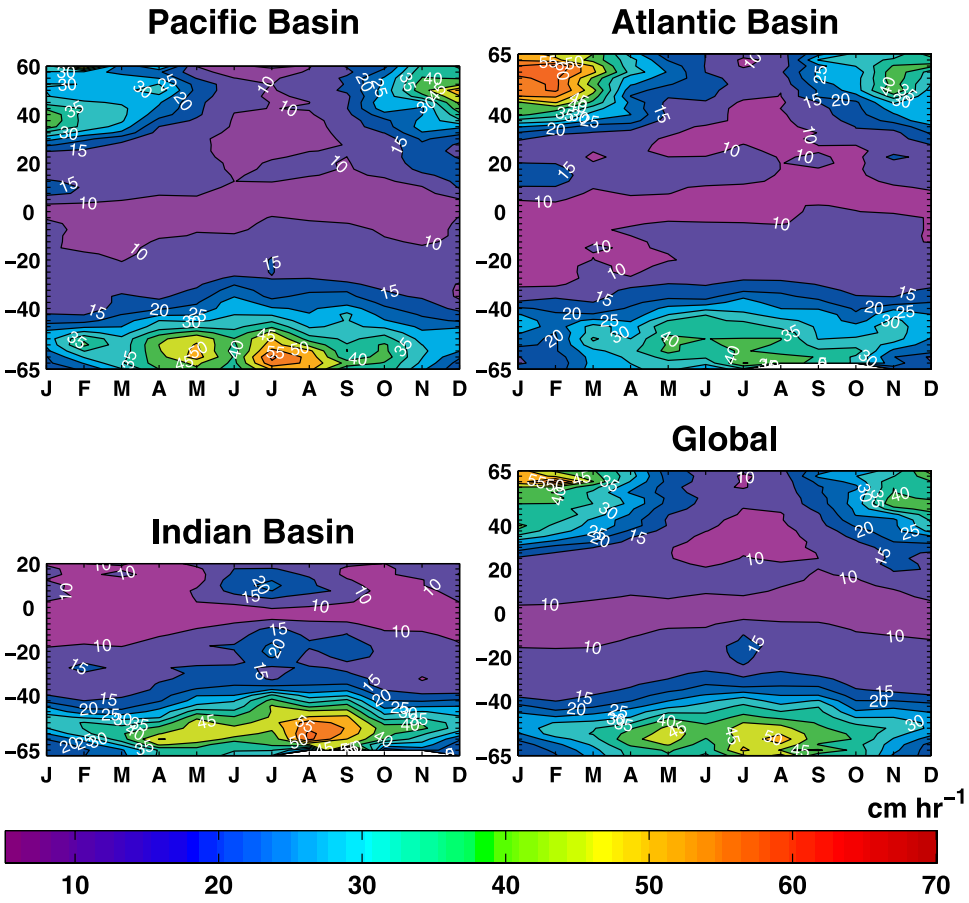

Figure 15. Seasonal variation of k_{660}, averaged on a zonal basis for the Pacific, Atlantic, and Indian Ocean basins and for the global ocean over the 2003 annual cycle.

recent estimates, is generally consistent with the bomb radiocarbon budget.

4.3.5. Algorithm Uncertainties and Limitations

[59] The algorithm described here is the first application of satellite microwave backscatter to the determination of global gas transfer velocity fields, via surface roughness and independent of wind speed. In this section we discuss uncertainties and limitations of the current version of the altimeter algorithm.

[60] A major uncertainty is the universality of k-$\langle s^2 \rangle_{40}^{100}$ relation (7); this remains to be established by more extensive field observations. The k-$\langle s^2 \rangle_{40}^{100}$ relation, and thus the final product of the algorithm, rests on a limited set of field observations made during CoOP97 [*Frew et al.*, 2004]. We make several points in this regard.

[61] First, the CoOP97 measurement methodology for gas transfer velocity was indirect: it relied on thermographic estimates of the ocean skin-bulk temperature difference using the surface renewal model, micrometeorological measurements of heat flux, and Schmidt number scaling [*Schimpf et al.*, 2004] of estimated heat transfer velocities to get gas transfer velocities. As noted in section 3.2, the use of various infrared techniques to estimate and extrapolate heat transfer velocities to gas transfer velocities assuming surface renewal is controversial. Recent experimental studies using the 'active controlled flux technique' (ACFT) to compare gas and heat fluxes across the air-water interface [*Asher et al.*, 2004; *Atmane et al.*, 2004] have cast doubt on use of the surface renewal model to represent turbulent interfacial transfer of heat and a gas due to the disparate diffusive length scales of these two tracers. These authors have promoted a random eddy model based on surface penetration theory [*Harriott*, 1962] in which eddies are not required to completely renew the water surface. In the surface penetration model, the straightforward Schmidt number scaling based on molecular diffusivities (or Prandtl number in the case of heat) is complicated by an additional dependence on the characteristics of the near-surface turbulence (eddy penetration depth and eddy lifetime). *Asher et al.* [2004] demonstrated that ACFT may overestimate gas transfer velocities by a factor of two. We note, however, that the scaled CoOP97 gas transfer velocities [*Frew et al.*, 2004] (obtained as described above, not by ACFT), do not appear to be anomalously high (certainly not by a factor of two) and in fact, give rise to a k-U_{10} relationship [*Frew et al.*, 2004] that is nearly identical to that of *Nightingale et al.* [2000b], which was derived from He/SF_6 dual-tracer studies. Nevertheless, additional confirmation of (7) with direct gas flux measurements remains a significant need.

[62] Second, while the CoOP97 observations included both coastal and oligotrophic waters, the algorithm would benefit from observations from a broader selection of ocean regions and over a wider range of physical forcing conditions. In particular, the accuracy of the algorithm in the

high-wind regime has not been determined. The mean square slope and gas transfer velocity observations during CoOP97 were limited to wind speeds of <10 m s^{-1} and the algorithm is thus an extrapolation for higher winds. The behavior of small-scale wave slope as wind speed increases above 10 m s^{-1} is uncertain since mean square slope measurements at higher winds are difficult to make and relatively few measurements of $\langle s^2 \rangle$ in high winds are available. Clearly, further refinement of the algorithm will benefit from additional field measurements of mean square slope and transfer velocities under a wider range of forcing conditions than is currently reported.

[63] Third, some subsurface processes contributing to gas transfer are not reflected in the mean square slope. The mean square slope approach does not account for enhancement of gas transfer at low winds by buoyancy flux effects such as diurnal stratification and overturning of the shallow mixed layer [*Soloviev and Schluessel*, 1996; *McGillis et al.*, 2004]. The dependence of gas transfer on mean square slope for high-wind, energetic sea states with breaking waves and bubbles is not established. The algorithm does not explicitly include a physics-based formulation of bubble-mediated effects due to breaking waves which may be significant for relatively insoluble gases [*Woolf and Thorpe*, 1991; *Woolf*, 1997; *Asher and Wanninkhof*, 1998; *Soloviev and Schluessel*, 2002]. It assumes a Schmidt number exponent $n = -0.5$ (equation (2)), which may not apply at higher wind speeds when bubble effects can be significant. The algorithm may implicitly include some breaking wave contribution due to the effects of whitecapping on normalized backscatter as evidenced by a slope change in the backscatter-wind speed relationship reported by *Chapron et al.* [1995]. However, the algorithm performance for energetic sea states could be improved by explicitly including a sea-state-dependent parameterization of bubble-enhanced exchange as suggested by *Woolf* [2005] and *Fangohr and Woolf* [2007].

[64] While the use of (7) results in gas transfer velocities that agree reasonably well with limited ground truth data and with other estimates of global average transfer velocity, its generalization to the global ocean must be considered tentative. The accumulation of calibration data sufficient to establish an operational remote sensing product based on mean square slope is a significant challenge. It will be difficult to put bounds on the k-$\langle s^2 \rangle$ relationship strictly using matchups of satellite and shipboard observations. Shipboard measurements of mean square slope using radars in conjunction with gas flux measurements could well accelerate this process. Ultimately, however, any calibration established using ship-based radars will need to be checked for problems scaling up to satellite radars and this can only be done with satellite-ground matchups.

[65] The algorithm may include additional biases relating to the elimination of rain events and the narrow swath, 10-day repeat ground track of the altimeter. Exclusion of rain-contaminated data may bias our results toward lower average k, particularly in regions of high rainfall. Rain flag characteristics and rain probabilities for TOPEX and Jason-1 have been extensively reported [*Tournadre and Morland*, 1997; *Quartly et al.*, 1999; *McMillan et al.*, 2002; *Quartly*, 2004; *Tournadre*, 2004, 2005]. The mean probability of rain is around 4%; however, in some areas, for example, the warm pool, this can reach 10–15% [*Tournadre*, 2005]. Increased winds are often associated with rain events and elimination of rain flagged data presumably should lead to a bias toward lower k estimates with a geographical distribution corresponding to major rainfall patterns. Rainfall itself may enhance gas transfer rates; such enhancement has been observed in laboratory experiments with freshwater systems by *Ho et al.* [2000]; however, the applicability of their conclusions to rainfall on the ocean surface is uncertain and we are not aware of oceanic data documenting or quantifying this effect. The situation is further complicated by the damping effect of rain on small-scale waves [reported by *Tsimplis and Thorpe*, 1989] which would enhance the Ku backscatter [*Guymer et al.*, 1995; *Quartly et al.*, 1996], possibly leading to missed rain events. Owing to the complexity of processes involved and the lack of an independent global database of mean square slope to which the altimeter data could be compared, we have no way of estimating the rain flag bias at this time. It is important to realize that a similar limitation applies to scatterometer wind retrievals [*Milliff et al.*, 2004]. Ku-band scatterometers (such as QuikSCAT SeaWinds) cannot provide valid vector wind estimates where it is raining, since the emitted pulse and backscattered radiation are attenuated by rain. In addition, rain alters the surface roughness, which also skews the backscatter-wind speed relationship such that the retrieval algorithm is invalid [*Milliff et al.*, 2004]. Thus a rain flag is also used for during QuikSCAT Seawinds processing to discard observations contaminated by rain, introducing bias.

[66] The restricted spatiotemporal coverage of altimeters is a significant limitation of our approach. The narrow-swath exact repeat ground track and 10-day cycle of the TOPEX and Jason-1 altimeters limit the algorithm basic product to monthly maps of k at 2.5° resolution. The orbit of the TOPEX/POSEIDON satellite results in ground tracks with an equatorial cross-track separation of 315 km and an exact repeat period of 9.9156 days. Since the spacing and period of these ground tracks are greater than the synoptic space and timescales of large, organized atmospheric eddies (fronts and storms), some variability of gas exchange driven by these atmospheric events will be undersampled. In order to avoid aliasing our results we have calculated average transfer velocities on a monthly 2.5° grid; effectively each grid cell has multiple k values averaged over three cycles. Nevertheless, bias from undersampling remains and our global long-term, area-weighted, Schmidt number adjusted mean transfer velocity of 13.7 ± 4.1 cm h^{-1} should be considered a lower limit. Observation of short-term variability and mesoscale spatial features in the global gas transfer velocity field could be improved with multiple altimeters in orbit. The extension of our mean square slope approach to scatterometer data is a promising avenue of research [*Glover et al.*, 2003, 2004] that also would provide better spatiotemporal coverage.

5. Conclusions

[67] An algorithm constructed using empirical observations of the dependence of gas transfer velocity on mean square slope, coupled with estimates of mean square slope from altimeter normalized backscatter and a geometric

optics scattering model produces estimates of transfer velocity that are generally consistent with $k - U_{10}$ parameterizations based on local-scale shipboard measurements and with estimates of the global average transfer velocity based on ocean bomb ^{14}C inventories. The algorithm generates estimates of k at 1-s resolution (~7-km spatial resolution) along the altimeter ground track and monthly global k fields at 2.5° resolution. Given the excellent quality of the TOPEX and Jason-1 data sets, the algorithm has the potential to provide a long, consistent record of gas transfer rates on a global scale [*Glover et al.*, 2007] and represents an important step in the determination of gas transfer rates via remotely sensed surface roughness.

Appendix A: Correction of TOPEX Normalized Backscatter for Atmospheric Attenuation

[68] Atmospheric attenuation corrections to both σ_0^{Ku} and σ_0^C were implemented incorrectly in the original TOPEX MGDR. These errors were only partially remedied in *Benada* [1997] and carried through to the GDR (see additional discussion by *Elfouhaily et al.* [1998]). Using the TOPEX GDR, the following correction calculations are necessary (note that, to avoid ambiguity, we have preserved the notation and variable naming conventions used in the TOPEX MGDR documentation [*Benada*, 1997]):

A1. Calculation of Vapor-Induced Path Delay (P_v) in Centimeters

[69]

$$P_v = -Wet\_H\_Rad/10 - 1.6L_z/10000$$

A2. Calculation of Integrated Liquid Water Content (L_z) in Microns

[70]

$$L_z = -2280.360 - 12.241(Tb\_18) - 5.128(Tb\_21) + 28.964(Tb\_37)$$

where *Tb*_18, *Tb*_21 and *Tb*_37 are the TOPEX Microwave Radiometer (TMR) brightness temperatures at 18, 21 and 37 GHz, respectively. If $L_z > 600$, then an additional adjustment is made:

$$L_z = L_z + L_{cor}$$

where

$$L_{cor} = 0.43(L_z - 600) + 0.0003(L_z - 600)^2$$

A3. Calculation of Corrected Sigma0_K in dB

[71]

$$Sigma0\_K(corrected) = Sigma\_K(\mathrm{GDR}) - Atm\_Att\_Sig0\_cor(\mathrm{GDR}) + Atm\_Att\_K$$

where *Atm_Att_K* is the two-way atmospheric attenuation correction in dB:

$$Atm\_Att\_K = 2(10\log_{10} e^{**}(0.01362 + 0.000514P_v + 0.32896L_z))$$

A4. Calculation of Corrected Sigma0_C in dB

[72]

$$Sigma0\_C(\mathrm{corrected}) = Sigma\_C(\mathrm{GDR}) - Atm\_Att\_Sig0\_cor(\mathrm{GDR}) + Atm\_Att\_C$$

where *Atm_Att_C* is the two-way atmospheric attenuation correction in dB:

$$Atm\_Att\_C = 2(10\log_{10} e^{**}(0.00987 + 0.0000217P_v + 0.05187L_v))$$

[73] Note that the σ_0^C atmospheric attenuation correction in the Jason-1 GDR is implemented only as a one-way correction and therefore must be multiplied by two.

[74] **Acknowledgments.** Financial support for this research from the National Aeronautics and Space Administration through Jet Propulsion Laboratory contract 961425 and the NOAA Global Carbon Cycle Program under grant NA16GP2918, Office of Global Programs is gratefully acknowledged. We wish to thank Tetsu Hara of the University of Rhode Island for making available the wave slope spectra from the 1997 CoOP Coastal Air-Sea Chemical Fluxes Experiment. Special thanks are owed to Kelley Case and Philip Callahan at the JPL/PO.DAAC for all of their assistance with the altimetry data sets. We would also like to thank Michael Caruso at WHOI for the initial use of his altimetry processing software and Ivan Lima and Scott Doney at WHOI for supplying Schmidt number adjusted gas transfer velocities using temperature and salinity fields from their OGCM simulations. We would also like to thank the Associate Editor, Wade McGillis, and two anonymous reviewers for their comments and suggestions for improving this paper. We note that Erik J. Bock, who began this project with us as a coinvestigator before his untimely death in June 2001, is included posthumously as an author on this manuscript.

References

Apel, J. R. (1994), An improved model of the ocean surface wave vector spectrum and its effects on radar backscatter, *J. Geophys. Res.*, *99*, 16,269–16,291.

Asher, W. E., and R. Wanninkhof (1998), The effect of bubble-mediated gas transfer on purposeful dual-gaseous tracer experiment, *J. Geophys. Res.*, *103*, 10,555–10,560.

Asher, W. E., Q. Wang, E. C. Monahan, and P. M. Smith (1998), Estimation of air-sea gas transfer velocities from apparent microwave brightness temperature, *Mar. Technol. Soc. J.*, *32*, 32–40.

Asher, W. E., A. T. Jessup, and M. A. Atmane (2004), Oceanic application of the active controlled flux technique for measuring air-sea transfer velocities of heat and gases, *J. Geophys. Res.*, *109*, C08S12, doi:10.1029/2003JC001862.

Atmane, M. A., W. E. Asher, and A. T. Jessup (2004), On the use of the active infrared technique to infer heat and gas transfer velocities at the air-water free interface, *J. Geophys. Res.*, *109*, C08S14, doi:10.1029/2003JC001805.

Back, D. D., and M. J. McCready (1988), Effect of small-wavelength waves on gas-transfer across the ocean surface, *J. Geophys. Res.*, *93*, 5143–5152.

Banner, M. L., and O. M. Phillips (1974), On the incipient breaking of small scale waves, *J. Fluid Mech.*, *65*, 647–656.

Benada, J. R. (1997), Merged GDR (TOPEX/POSEIDON) Generation B user's handbook, version 2.0, *JPL-D-11007*, 124 pp., Phys. Oceanogr. Distrib. Active Archive Cent., Jet Propul. Lab., Calif. Inst. of Technol., Pasadena, Calif.

Bliven, L. F., P. Sobieski, A. Guissard, and H. Branger (1996), Friction velocity estimation using dual-frequency altimeter data, in *The Air-Sea*

Interface, edited by M. A. Donelan et al., pp. 755–760, Univ. of Toronto Press, Toronto, Ont., Canada.

Bock, E. J., and T. Hara (1995), Optical measurements of ripples using a scanning laser slope gauge, *J. Atmos. Oceanic Technol.*, *12*, 395–403.

Bock, E. J., and J. A. Mann Jr. (1989), On ripple dynamics. II. A corrected dispersion relation for surface waves in the presence of surface elasticity, *J. Colloid Interface Sci.*, *129*, 501–505.

Bock, E. J., et al. (1995), Description of the science plan for the April, 1995 CoOP experiment, "Gas Transfer in Coastal Waters," performed from the Research Vessel New Horizon, in *Air-Water Gas Transfer*, edited by B. Jähne and E. Monahan, pp. 801–810, AEON-Verlag, Hanau, Germany.

Bock, E. J., T. Hara, N. M. Frew, and W. R. McGillis (1999), Relationship between air-sea gas transfer and short wind waves, *J. Geophys. Res.*, *104*, 25,821–25,831.

Bösinger, R. (1986), Messungen zur Schmidtzahlabhängigkeit des Gasaustausches, diploma thesis, 55 pp., Univ. of Heidelberg, Heidelberg, Germany.

Boutin, J., and J. Etcheto (1995), Estimating the chemical enhancement effect on the air-sea CO_2 exchange using the ERS1 scatterometer wind speeds, in *Air-Water Gas Transfer*, edited by B. Jähne and E. Monahan, pp. 827–841, AEON-Verlag, Hanau, Germany.

Boutin, J., et al. (1999), Satellite sea surface temperature: A powerful tool for interpreting in situ pCO_2 measurements in the equatorial Pacific Ocean, *Tellus, Ser. B*, *51*, 490–508.

Boutin, J., J. Etcheto, L. Merlivat, and Y. Rangama (2002), Influence of gas exchange coefficient parameterisation on seasonal and regional variability of CO_2 air-sea fluxes, *Geophys. Res. Lett.*, *29*(8), 1182, doi:10.1029/2001GL013872.

Bowles, F. A., P. R. Vogt, and W.-Y. Jung (1998), Bathymetry (Part I), sedimentary regimes (Part II) and abyssal waste-disposal potential near the coterminous United States, *J. Mar. Syst.*, *14*, 211–239.

Broecker, W. S., J. R. Ledwell, T. Takahashi, R. Weiss, L. Merlivat, L. Memery, T. H. Peng, B. Jähne, and K. O. Munnich (1986), Isotopic versus micrometeorologic ocean CO_2 fluxes: A serious conflict, *J. Geophys. Res.*, *91*, 10,517–10,527.

Brown, G. S. (1990), Quasi-specular scattering from the air-sea interface, in *Surface Waves and Fluxes*, vol. II, edited by G. Geernaert and W. Plant, pp. 1–40, Springer, New York.

Chapron, B., K. Katsaros, T. Elfouhaily, and D. Vandemark (1995), A note on relationships between sea surface roughness and altimeter backscatter, in *Air-Water Gas Transfer, Selected Papers from the Third International Symposium on Air-Water Gas Transfer July 24–27, 1995*, edited by B. Jähne and E. C. Monahan, pp. 869–878, AEON Verlag and Studio, Hanau, Germany.

Chelton, D. B., J. C. Ries, B. J. Haines, L.-L. Fu, and P. S. Callahan (2001), Satellite altimetry, in *Satellite Altimetry and Earth Sciences, A Handbook of Techniques and Applications*, edited by L.-L. Fu and A. Cazenave, pp. 1–132, Academic Press, San Diego, Calif.

Coantic, M. (1986), A model of gas-transfer across air-water interfaces with capillary waves, *J. Geophys. Res.*, *91*, 3925–3943.

Cox, C., and W. Munk (1954), Statistics of the sea surface derived from sun glitter, *J. Mar. Res.*, *13*(2), 198–227.

Csanady, G. T. (1990), The role of breaking wavelets in air-sea gas-transfer, *J. Geophys. Res.*, *95*, 749–759.

Davis, J. C. (1986), *Statistics and Data Analysis in Geology*, 646 pp., John Wiley, Hoboken, N. J.

Edson, J. B., A. A. Hinton, K. E. Prada, J. E. Hare, and C. W. Fairall (1998), Direct covariance flux estimates from mobile platforms at sea, *J. Atmos. Oceanic Technol.*, *15*, 547–562.

Elfouhaily, T., B. Chapron, V. Kerbaol, J. Gourrion, J. Tournadre, K. Katsaros, and V. Vandemark (1996), Dependence of altimeter returns on wind stress and wave age, in *Proceedings of International Geoscience and Remote Sensing Symposium*, vol. II, pp. 1389–1391, IEEE Press, Piscataway, N. J.

Elfouhaily, T., B. Chapron, K. Katsaros, and D. Vandemark (1997), A unified directional spectrum for long and short wind-driven waves, *J. Geophys. Res.*, *102*, 15,781–15,796.

Elfouhaily, T., D. Vandemark, J. Gourrion, and B. Chapron (1998), Estimation of wind stress using dual-frequency TOPEX data, *J. Geophys. Res.*, *103*, 25,101–25,108.

Emery, W. J., D. G. Baldwin, and D. K. Matthews (2004), Sampling the mesoscale ocean surface currents with various satellite altimeter configurations, *IEEE Trans. Geosci. Remote Sens.*, *42*, 795–803.

Erikson, D. J., III (1993), A stability dependent theory for air-sea gas exchange, *J. Geophys. Res.*, *98*, 8471–8488.

Etcheto, J., and L. Merlivat (1988), Satellite determination of the carbon dioxide exchange coefficient at the ocean-atmosphere interface: A first step, *J. Geophys. Res.*, *93*, 15,669–15,678.

Fairall, C. W., J. E. Hare, J. B. Edson, and W. R. McGillis (2000), Parameterization and micro-meteorological measurement of air-sea transfer, *Boundary Layer Meteorol.*, *96*, 63–105.

Fangohr, S., and D. K. Woolf (2007), Application of new parameterizations of gas transfer velocity and their impact on regional and global marine CO_2 budgets, *J. Mar. Syst.*, *66*, 195–203.

Freilich, M. H., and B. A. Vanhoff (2003), The relationship between winds, surface roughness, and radar backscatter at low incidence angles from TRMM precipitation radar measurements, *J. Atmos. Oceanic Technol.*, *20*, 549–562.

Frew, N. M. (1997), The role of organic films in air-sea gas exchange, in *The Sea Surface and Global Change*, edited by P. Liss and R. Duce, pp. 121–172, Cambridge Univ. Press, New York.

Frew, N. M., and R. K. Nelson (1999), Spatial mapping of sea surface microlayer surfactant concentration and composition, in *Proceedings of the 1999 International Geoscience and Remote Sensing Symposium*, edited by T. I. Stein, pp. 1472–1474, IEEE Press, Piscataway, N. J.

Frew, N. M., J. C. Goldman, M. R. Dennett, and A. S. Johnson (1990), The impact of phytoplankton-generated surfactants on gas exchange at the air-sea interface, *J. Geophys. Res.*, *95*, 3337–3352.

Frew, N. M., E. J. Bock, W. R. McGillis, A. V. Karachintsev, T. Hara, T. Münsterer, and B. Jähne (1995), Variation of air-water gas transfer with wind stress and surface viscoelasticity, in *Air-Water Gas Transfer*, edited by B. Jähne and E. C. Monahan, pp. 529–541, AEON Verlag, Hanau, Germany.

Frew, N. M., D. M. Glover, E. J. Bock, S. McGillis, W. R. McCue, and R. Healy (1997), Satellite estimation of gas transfer velocity using altimeter backscatter, *Eos Trans. AGU*, *78*(17), Spring Meet Suppl., S88.

Frew, N. M., E. J. Bock, W. R. McGillis, J. B. Edson, and T. Hara (2002), Spatial variations in surface microlayer surfactants and their role in modulating air-sea exchange, in *Gas Transfer at Water Surfaces*, *Geophys. Monogr. Ser.*, vol. 127, edited by M. A. Donelan et al., pp. 153–159, AGU, Washington, D. C.

Frew, N. M., et al. (2004), Air-sea gas transfer: Its dependence on wind stress, small-scale roughness, and surface films, *J. Geophys. Res.*, *109*, C08S17, doi:10.1029/2003JC002131.

Gemmrich, J., and L. Hasse (1992), Small-scale surface streaming under natural conditions as effective in air-sea gas exchange, *Tellus, Ser. B*, *44*, 150–159.

Glover, D. M., N. M. Frew, S. J. McCue, and E. J. Bock (2002), A multiyear time series of global gas transfer velocity from the TOPEX dual frequency, normalized radar backscatter algorithm, in *Gas Transfer at Water Surfaces*, *Geophys. Monogr. Ser.*, vol. 127, edited by M. A. Donelan et al., pp. 325–331, AGU, Washington, D. C.

Glover, D. M., M. J. Caruso, N. M. Frew, and S. J. McCue (2003), Derivation of air-sea gas transfer velocities from QuikSCAT using co-located normalized radar backscatter from TOPEX, *Eos Trans. AGU*, *84*(52), Ocean Sci. Meeting Suppl., Abstract OS13B-0533.

Glover, D. M., N. M. Frew, M. J. Caruso, and S. J. McCue (2004), Prediction of gas exchange rate using microwave backscatter from the ocean surface, *Eos Trans. AGU*, *85*(47), Fall Meeting Suppl., Abstract OS13B-0533.

Glover, D. M., N. M. Frew, and S. J. McCue (2007), Air-sea gas transfer velocity estimates from the Jason-1 and TOPEX altimeters: Prospects for a long-term global time series, *J. Mar. Syst.*, *66*, 173–181.

Gommenginger, C. M., M. Srokosz, P. Challenor, and P. Cotton (2002), Development and validation of altimeter wind speed algorithms using an extended collocated buoy/TOPEX dataset, *IEEE Trans. Geosci. Remote Sens.*, *40*, 251–260.

Gourrion, J., D. Vandemark, S. Bailey, B. Chapron, G. P. Gommenginger, P. G. Challenor, and M. A. Srokosz (2002), A two-parameter wind speed algorithm for Ku-band altimeters, *J. Atmos. Oceanic Technol.*, *19*, 2030–2048.

Guymer, T. H., G. D. Quartly, and M. A. Srokosz (1995), The effects of rain on ERS-1 radar altimeter data, *J. Atmos. Oceanic Technol.*, *12*, 1229–1247.

Hara, T., E. J. Bock, N. M. Frew, and W. R. McGillis (1995), Relationship between air-sea gas transfer velocity and surface roughness, in *Air-Water Gas Transfer*, edited by B. Jähne and E. C. Monahan, pp. 611–616, AEON Verlag, Hanau, Germany.

Hara, T., E. J. Bock, J. B. Edson, and W. R. McGillis (1998), Observations of short wind waves in coastal waters, *J. Phys. Oceanogr.*, *28*, 1425–1438.

Harriott, P. (1962), A random eddy modification of the penetration theory, *Chem. Eng. Sci.*, *17*, 149–154.

Haußecker, H. (1996), Measurements and simulation of small scale exchange processes at the ocean surface, Ph.D. thesis, 203 pp., Univ. of Heidelberg, Heidelberg, Germany.

Ho, D. T., W. E. Asher, L. F. Bliven, P. Schlosser, and E. L. Gordan (2000), On mechanisms of rain-induced air-water gas exchange, *J. Geophys. Res.*, *105*, 24,045–24,057.

Jackson, F. C., W. T. Walton, D. E. Hines, B. A. Walter, and C. Y. Peng (1992), Sea surface mean square slope from Ku-band backscatter data, *J. Geophys. Res.*, *97*, 11,411–11,427.

Jähne, B. (1985), Transfer processes across the free water surface, Habilitation thesis, 136 pp., Univ. of Heidelberg, Heidelberg, Germany.
Jähne, B., and H. Haußecker (1998), Air-water gas exchange, Annu, *Rev. Fluid Mech.*, *30*, 443–468.
Jähne, B., K. O. Münnich, and U. Siegenthaler (1979), Measurements of gas exchange and momentum transfer in a circular wind-water tunnel, *Tellus*, *31*, 321–329.
Jähne, B., W. Huber, A. Dutzi, T. Wais, and J. Ilmberger (1984), Wind/wave-tunnel experiment on the Schmidt number and wave field dependence of air/water gas exchange, in *Gas Transfer at Water Surfaces*, edited by W. Brutsaert and G. H. Jirka, pp. 303–309, Springer, New York.
Jähne, B., K. O. Münnich, R. Bösinger, A. Dutzi, W. Huber, and P. Libner (1987), On the parameters influencing air-water gas exchange, *J. Geophys. Res.*, *92*, 1937–1949.
Jessup, A. T., C. J. Zappa, and H. Yeh (1997), Defining and quantifying microscale wave breaking with infrared imagery, *J. Geophys. Res.*, *102*, 23,145–23,153.
Katsaros, K. B., and S. S. Attaturk (1992), Dependence of wave-breaking statistics on wind stress and wave development, in *Breaking Waves: IUTAM Symposium, Sidney Australia, 1991*, edited by M. L. Banner and R. H. J. Grimshaw, pp. 119–132, Springer, New York.
Liss, P. S., and L. Merlivat (1986), Air-sea gas exchange rates: Introduction and synthesis, in *The Role of Air-Sea Exchange in Geochemical Cycling*, edited by P. Buat-Menard, pp.113–127, Springer, New York.
Liu, Y., M.-Y. Su, X.-H. Yan, and W. T. Liu (2000), The mean square slope of ocean surface waves and its effects on radar backscatter, *J. Atmos. Oceanic. Technol.*, *17*, 1092–1105.
Lockwood, D. W., D. W. Hancock III, G. S. Hayne, and R. L. Brooks (2005), TOPEX radar altimeter engineering assessment report update Side B turn-on to January 1, 2005, *NASA/TM-2005-212236*, NASA/GSFC Wallops Flight Facil., Wallops Island, Va.
MathWorks (2000), *Optimization Toolbox, User's Guide version 2.1*, 332 pp., MathWorks, Natick, Mass.
McGillis, W. R., J. B. Edson, J. E. Hare, and C. W. Fairall (2001a), Direct covariance of air-sea CO_2 fluxes, *J. Geophys. Res.*, *106*, 16,729–16,745.
McGillis, W. R., J. B. Edson, J. D. Ware, J. W. H. Dacey, J. E. Hare, C. W. Fairall, and R. Wanninkhof (2001b), Carbon dioxide flux techniques performed during GasEx-98, *Mar. Chem.*, *75*, 267–280.
McGillis, W. R., et al. (2004), Air-sea CO_2 exchange in the equatorial Pacific, *J. Geophys. Res.*, *109*, C08S02, doi:10.1029/2003JC002256.
McMillan, A. C., G. D. Quartly, and M. A. Srokosz (2002), Validation of the TOPEX rain algorithm: Comparison with ground-based radar, *J. Geophys. Res.*, *107*(D4), 4038, doi:10.1029/2001JD000872.
Melville, W. K., R. Shear, and F. Veron (1998), Laboratory measurements of the generation and evolution of Langmuir circulations, *J. Fluid Mech.*, *364*, 31–58.
Milliff, R. F., J. Morzel, D. B. Chelton, and M. H. Freilich (2004), Wind stress curl and wind stress divergence biases from rain effects on QSCAT surface wind retrievals, *J. Atmos. Oceanic Technol.*, *21*, 1216–1231.
Mitchum, G. T., D. W. Hancock III, G. S. Hayne, and D. C. Vandemark (2004), Blooms of σ_0 in the TOPEX radar altimetry data, *J. Atmos. Oceanic Technol.*, *21*, 1232–1245.
Moore, J. K., S. C. Doney, and K. Lindsay (2004), Upper ocean ecosystem dynamics and iron cycling in a global three-dimensional model, *Global Biogeochem. Cycles*, *18*, GB4028, doi:10.1029/2004GB002220.
Naegler, T., P. Ciais, K. Rodgers, and I. Levin (2006), Excess radiocarbon constraints on air-sea gas exchange and the uptake of CO_2 by the oceans, *Geophys. Res. Lett.*, *33*, L11802, doi:10.1029/2005GL025408.
Nightingale, P. D., P. S. Liss, and P. Schlosser (2000a), Measurements of air-sea gas transfer during an open ocean algal bloom, *Geophys. Res. Lett.*, *27*, 2117–2120.
Nightingale, P. D., G. Malin, C. S. Law, A. J. Watson, P. S. Liss, M. I. Liddicoat, J. Boutin, and R. C. Upstill-Goddard (2000b), In situ evaluation of air-sea gas exchange parameterizations using novel conservative and volatile tracers, *Global Biogeochem. Cycles*, *14*, 373–387.
Olsen, A., R. Wanninkhof, J. A. Triñanes, and T. Johannessen (2005), The effect of wind speed products and wind-speed-gas exchange relationships on interannual variability of the air-sea CO_2 gas transfer velocity, *Tellus, Ser. B*, *57*, 95–106.
Peirson, W. L., and M. L. Banner (2003), Aqueous surface layer flows induced by microscale breaking wind waves, *J. Fluid Mech.*, *479*, 1–38.
Picot, N., K. Case, S. Desai, and P. Vincent (2006), AVISO and PODAAC User Handbook: IGDR and GDR Jason Products, ed. 3.0, *SMM-MU-M5-OP-13184-CN (AVISO)*, Cent. Nat. d'Etudes Spatiales, Toulouse, France. (Available at http://www.jason.oceanobs.com/documents/donnees/tools/handbook_jason.pdf)
Quartly, G. D. (2004), Sea state and rain: A second take on dual-frequency altimetry, *Mar. Geod.*, *27*, 133–152.
Quartly, G. D., T. H. Guymer, and M. A. Srokosz (1996), The effects of rain on TOPEX radar altimeter data, *J. Atmos. Oceanic Technol.*, *13*, 1209–1229.
Quartly, G. D., M. A. Srokosz, and T. H. Guymer (1999), Global precipitation statistics from dual-frequency TOPEX altimetry, *J. Geophys. Res.*, *104*, 31,489–31,516.
Ruf, C. S. (2002), Characterization and correction of a drift in calibration of the TOPEX microwave radiometer, *IEEE Trans. Geosci. Remote Sens.*, *40*, 509–511.
Schimpf, U., B. Jähne, and H. Haußecker (2002), On the investigation of statistical properties of the micro turbulence at the ocean surface, in *Gas Transfer at Water Surfaces*, *Geophys. Monogr. Ser.*, vol. 127, edited by M. A. Donelan et al., pp. 51–57, AGU, Washington, D. C.
Schimpf, U., S. Garbe, and B. Jähne (2004), Investigation of the transport process across the sea-surface microlayer by infrared imagery, *J. Geophys. Res.*, *109*, C08S13, doi:10.1029/2003JC001803.
Schmundt, D., T. Münsterer, H. Lauer, and B. Jähne (1995), The circular wind-wave facility at the University of Heidelberg, in *Selected Papers from the Third International Symposium on Air-Water Gas Transfer*, edited by B. Jähne and E. C. Monahan, pp. 505–516, Aeon Verlag, Hanau, Germany.
Siddiqui, M. H. K., M. R. Loewen, C. Richardson, W. E. Asher, and A. T. Jessup (2001), Simultaneous particle image velocimetry and infrared imagery of microscale breaking waves, *Phys. Fluids*, *13*, 1891–1903.
Soloviev, A. V., and P. Schlüssel (1994), Parameterization of the cool skin of the ocean and of the air-ocean gas transfer on the basis of modeling surface renewal, *J. Phys. Oceanogr.*, *24*, 1339–1346.
Soloviev, A. V., and P. Schluessel (1996), Evolution of cool skin and direct air-sea gas transfer coefficient during daytime, *Boundary Layer Meteorol.*, *77*, 45–68.
Soloviev, A. V., and P. Schluessel (2002), A model of air-sea gas exchange incorporating the physics of the turbulent boundary layer and the properties of the sea surface, in *Gas Transfer at Water Surfaces*, *Geophys. Monogr. Ser.*, vol. 127, edited by M. A. Donelan et al., pp. 141–146, AGU, Washington, D. C.
Sweeney, C., E. Gloor, A. R. Jacobson, R. M. Key, G. McKinley, J. L. Sarmiento, and R. Wanninkhof (2007), Constraining global air-sea gas exchange for CO_2 with recent bomb ^{14}C measurements, *Global Biogeochem. Cycles*, *21*, GB2015, doi:10.1029/2006GB002784.
Takahashi, T., et al. (2002), Global sea-air CO_2 flux based on climatological surface ocean pC02, and seasonal biological and temperature effects, *Deep Sea Res., Part II*, *49*, 1601–1623.
Tans, P. P., I. Y. Fung, and T. Takahashi (1990), Observational constraints on the global atmospheric CO_2 budget, *Science*, *247*, 1431–1438.
Tournadre, J. (2004), Validation of Jason and Envisat altimeter dual frequency rain flags, *Mar. Geod.*, *27*, 153–169.
Tournadre, J. (2005), Level 3 rain products from dual frequency altimeters—Rain-ALT products, *User Manual IFREMER C2-MUT-RAIN-01-1F*, 49 pp, Inst. Français de Rech. pour l'Exploitation de la Mer, Plouzane, France.
Tournadre, J., and J. Morland (1997), The effect of rain on TOPEX/POSEIDON altimeter data: A new rain flag on Ku and C band backscatter coefficients, *IEEE Trans. Geosci. Remote Sens.*, *35*, 1117–1135.
Tournadre, J., B. Chapron, N. Reul, and D. C. Vandemark (2006), A satellite altimeter model for ocean slick detection, *J. Geophys. Res.*, *111*, C04004, doi:10.1029/2005JC003109.
Tsimplis, M., and S. A. Thorpe (1989), Wave damping by rain, *Nature*, *342*, 893–895.
Vandemark, D., J. B. Edson, and B. Chapron (1997), Altimeter estimation of sea surface wind stress for light to moderate winds, *J. Atmos. Oceanic Technol.*, *14*, 716–722.
Wanninkhof, R. (1992), Relationship between wind speed and gas exchange over the ocean, *J. Geophys. Res.*, *97*, 7373–7382.
Wanninkhof, R., and W. R. McGillis (1999), A cubic relationship between gas transfer and wind speed, *Geophys. Res. Lett.*, *26*, 1889–1893.
Wanninkhof, R., S. C. Doney, T. Takahashi, and W. R. McGillis (2002), The effect of using time-averaged winds on regional air-sea CO_2 fluxes, in *Gas Transfer at Water Surfaces*, *Geophys. Monogr. Ser.*, vol. 127, edited by M. A. Donelan et al., pp. 351–356, AGU, Washington, D. C.
Woolf, D. K. (1997), Bubbles and their role in gas exchange, in *The Sea Surface and Global Change*, edited by P. Liss and R. Duce, pp. 173–1205, Cambridge Univ. Press, New York.
Woolf, D. K. (2005), Parametrization of gas transfer velocities and sea-state-dependent wave breaking, *Tellus, Ser. B*, *57*, 87–94.
Woolf, D. K., and S. A. Thorpe (1991), Bubbles and the air-sea exchange of gases in near-saturation conditions, *J. Mar. Res.*, *49*, 435–466.
York, D., N. M. Evensen, M. L. Martinez, and J. D. B. Delgado (2004), Unified equations for the slope, intercept, and standard errors of the best straight line, *Am. J. Phys.*, *72*, 367–375.

Zappa, C. J. (1999), Microscale wave breaking and its effect on air-water gas transfer using infrared imagery, Ph.D. thesis, Appl. Phys. Lab., Univ. of Wash., Seattle.

Zappa, C. J., W. E. Asher, and A. T. Jessup (2001), Microscale breaking and air-water gas transfer, *J. Geophys. Res.*, *106*, 9385–9391.

Zappa, C. J., W. E. Asher, A. T. Jessup, J. Klinke, and S. R. Long (2002), Effect of microscale wave breaking on air-water gas transfer, in *Gas Transfer at Water Surfaces*, *Geophys. Monogr. Ser.*, vol. 127, edited by M. A. Donelan et al., pp. 23–29, AGU, Washington, D. C.

N. M. Frew, D. M. Glover, and S. J. McCue, Woods Hole Oceanographic Institution, 360 Woods Hole Road, Woods Hole, MA 02543, USA. (nfrew@whoi.edu)